

Performance of a Solar Flat Plate Collector with Integrated Phase Change Storage

by

Weihang Luo

Department of Mechanical Engineering  
Duke University

Date: \_\_\_\_\_

Approved:

\_\_\_\_\_  
Josiah D. Knight, Supervisor

\_\_\_\_\_  
Donald B. Bliss

\_\_\_\_\_  
Adrian Bejan

\_\_\_\_\_  
Nico Hotz

Thesis submitted in partial fulfillment of  
the requirements for the degree of  
Master of Science in the Department of  
Mechanical Engineering and Material Science  
of Duke University

2019

ABSTRACT

Performance of a Solar Flat Plate Collector with Integrated Phase Change Storage

by

Weihang Luo

Department of Mechanical Engineering  
Duke University

Date: \_\_\_\_\_

Approved:

\_\_\_\_\_  
Josiah D. Knight, Supervisor

\_\_\_\_\_  
Donald B. Bliss

\_\_\_\_\_  
Adrian Bejan

\_\_\_\_\_  
Nico Hotz

An abstract of a thesis submitted in partial  
fulfillment of the requirements for the degree of  
Master of Science in the Department of  
Mechanical Engineering and Material Science  
of Duke University

2019

Copyright by  
Weihang Luo  
2019

## **Abstract**

The thesis documents the investigation of the time-dependent melting process of paraffin in a solar flat plate collector with integrated heat storage concept. Among all the aspects that affect the phase change, the internal convection effect is in primary attention. The investigation starts with the numerical approach, which provides valuable information to design validation experiments. An apparatus was built to test two reduced scale demonstrators, which are heated up by simulated insolation. To maintain incoming heat flux consistent, the experiments were completed in a laboratory environment where the insolation simulation is applied. The phase transition is recorded and analyzed from the observations and temperature readings in total four melting cycles.

This study validates the feasibility of combining solar energy collection and storage. The general trends of the calculation are confirmed by experiment results, an improved understanding of how the internal convection affects the phase change pattern has obtained. Although the numerical approach models the experiments as much as possible, differences in time response have emerged. Discussions regarding the gaps are made, but some remain inconclusive. To evaluate the comprehensive performances of the passive solar heat storage, recommendations regarding future investigations are made.

*To my parents.*

# Contents

Abstract .....	iv
List of Tables .....	viii
List of Figures .....	ix
Nomenclature .....	xi
Acknowledgements .....	xiii
1. Introduction .....	1
1.1 Thermophysical Properties .....	2
1.2 Modeling of Internal Convection Effect .....	4
1.3 Active Storage Versus Passive Storage .....	7
1.4 Geometry of a Passive Storage .....	9
1.4.1 Thickness of PCM Layer .....	10
1.5 A Scope of Present Work .....	11
2. Numerical Analysis .....	13
2.1 Computational Domain .....	13
2.1.1 Heat Loss Coefficient .....	15
2.2 Equations .....	18
2.3 Solver setup .....	20
2.4 Results .....	22
2.4.1 Phase Distribution .....	22
2.4.2 Liquid Fraction .....	26

2.4.3 Temperature and Velocity Distribution .....	27
2.4.4 Summary of Numerical Findings.....	30
3. Experiment Setup and Results .....	31
3.1 Material Properties from Differential Scanning Calorimetry.....	31
3.2 Integrated Phase Change Storage Demonstration Collector .....	34
3.3 Rig Tests.....	36
3.3.1 Radiation Heat Source .....	36
3.4 Experiment Results.....	39
3.4.1 Collector Vertical .....	39
3.4.2 Collector 60° Inclined.....	45
3.4.3 Thermocouple Readings.....	54
3.4.4 Comparison with Numerical Prediction.....	57
4. Conclusion .....	59
4.1 Recommendations for Future Work .....	60
References .....	61

## List of Tables

Table 1: The derived dimensionless numbers and convective heat transfer coefficient value by external natural convection correlations .....	17
Table 2: Thermophysical properties of n-tetracosane .....	20
Table 3: Phase change specified solver setup.....	21

## List of Figures

Figure 1: Blending higher alkanes: Latent heat of fusion variation of hexadecane-octadecane binary system.....	3
Figure 2: Comparison of different numerical techniques.....	6
Figure 3: Solid paraffin sinks in liquid. The mushy region is visible. ....	7
Figure 4: The proposed geometry and application of a solar flat plate collector integrated storage.....	9
Figure 5: The dimensions, boundary conditions, and the initial condition of the computational domain. ....	14
Figure 6: From left to right, mass fraction contour at $t = 10\text{min}$ , $t = 20\text{min}$ and $t = 30\text{min}$ . Contour enlarged in $x$ -direction by a factor of 5. ....	24
Figure 7: From left to right, mass fraction contour at $t = 40\text{min}$ , $t = 50\text{min}$ and $t = 60\text{min}$ . Contour enlarged in $x$ -direction by a factor of 5. ....	25
Figure 8: The predicted liquid fraction. ....	26
Figure 9: Isothermal and velocity contour at $t = 50\text{ min}$ (Vertical). Contour enlarged in $x$ -direction by a factor of 5.....	28
Figure 10: Streamlines and the velocity vectors in the mixing region.....	29
Figure 11: DSC curves. ....	33
Figure 12: The schematic of the reduced scale solar flat plate collector integrated storage demonstration module. Left: front view. Right: Cross-section .....	35
Figure 13: The tilted test rig. The demonstration collector on the right is clamped and inclined. The lamps at a fixed distance provide light beam normal to the front plate. ....	38
Figure 14: Solid-liquid boundary at $t = 40\text{ min}$ (Collector #2, vertical). Small amount of liquid phase appeared at the top. ....	40
Figure 15: Solid-liquid boundary at $t = 50\text{ min}$ (Collector #2, vertical). ....	41
Figure 16: Solid-liquid boundary at $t = 60\text{ min}$ (Collector #2, vertical). ....	42

Figure 17: Solid-liquid boundary at t = 70 min (Collector #2, vertical). .....	43
Figure 18: Solid-liquid boundary at t = 80 min (Collector #2, vertical). .....	44
Figure 19: Solid-liquid boundary at t = 60 min (Collector #2, 60° Inclined).....	46
Figure 20: Solid-liquid boundary at t = 70 min (Collector #2, 60° Inclined).....	47
Figure 21: Solid-liquid boundary at t = 80 min (Collector #2, 60° Inclined).....	48
Figure 22: Solid-liquid boundary at t = 90 min (Collector #2, 60° Inclined).....	49
Figure 23: Solid-liquid boundary at t = 100 min (Collector #2, 60° Inclined).....	50
Figure 24: Solid-liquid boundary at t = 110 min (Collector #2, 60° Inclined).....	51
Figure 25: Evolution of solid-liquid boundary between t = 40 min and t = 80 min. (Collector#2, vertical).....	52
Figure 26: Evolution of solid-liquid boundary between t = 60 min and t = 110 min (Collector#2, 60° inclined). .....	53
Figure 27: Temperature measurements of vertical oriented collector.....	55
Figure 28: Temperature measurements of 60-degree inclination oriented collector .....	56
Figure 29: Prediction and measurements of the solid-liquid boundary progression.....	58

## Nomenclature

$a, b$	Geometry dimensions of PCM
$A_{\text{mush}}$	Mushy zone constant
$g$	Gravitational acceleration ( $\text{m/s}^2$ )
$h$	Specific enthalpy ( $\text{J/kg}$ )
$\bar{h}$	Wall average external natural convective heat transfer coefficient
$k$	Thermal conductivity ( $\text{W}/(\text{m K})$ )
$l$	Latent heat ( $\text{kJ/kg}$ )
$t$	time
$T$	Temperature ( $\text{K}$ )
$\theta$	Angular orientation
$\beta$	Volumetric thermal expansion coefficient ( $1/\text{K}$ )
$\rho$	Density ( $\text{kg/m}^3$ )
$\varepsilon$	A positive number less than 0.001
$\mu$	Dynamic viscosity ( $\text{Pa}\cdot\text{s}$ )
$\nu$	Kinematic viscosity ( $\text{m}^2/\text{s}$ )
$S_u, S_v$	Momentum equation's source term
$S_h$	Energy equation's source term
$\lambda$	Porosity, $0 < \lambda < 1$
$\text{Pr}$	Prandtl number

Gr Grashof number

Ra Rayleigh number

$\overline{Nu}$  Wall average external natural convection Nusselt number

*Subscript*

*tot* Total

*sen* Sensible

*ref* Reference value

s Solidus

L Liquidous

## Acknowledgements

I would like to express the most special thanks of gratitude to my advisor Prof. Josiah D. Knight, who offered wisdom, experience and financial support for the study. I also would like to thank Professors Donald B. Bliss, Adrian Bejan, and Nico Hotz for their valuable advice.

I wish to thank Alexandra Zajda who has worked with me over a year. I appreciate Dr. Peter Silinski's support as I learned to use differential scanning calorimetry (DSC). I would like to acknowledge Yue Kang (康跃) for his assistance with access to China Academic Journal Network Publishing Database, and to thank Wentao Ma (马文韬) for his help with the finite volume software. Finally, I would like to express my gratitude to Ziyi Li (梓一哥), Ding Liao (廖总) and Pengyu Zhao (翘桑) for their consistent support for many years.

# 1. Introduction

Heat storage is frequently proposed in solar thermal engineering to balance the solar energy supply for the day/night cycle. Solar heat storage is always in a transient state of its periodic daily cycle, either charging with surplus solar energy or discharging for heating purpose. The desired characteristics of solar heat storage include the capability of storing a large amount of energy within the operating temperature range. Three common heat storage options that meet this requirement are sensible heat storage, latent heat storage and thermochemical storage [1][2].

Latent heat storage using phase change material (PCM) is a competitive solution, and paraffin is an excellent performer among PCM selections for multiple reasons. Paraffin is a mixture of alkanes which are solid at room temperature but undergo phase transformation at a temperature ideal for solar heating. The latent heat of fusion during phase change gives the latent heat storage high energy density, which further improves the compactness. The quality of paraffin does not degrade after repeated cycles or exposure to moisture [35]. Other properties that also show paraffin's effectiveness as a heat storage material include being lightweight, non-toxic and non-corrosive [3].

The studies of PCM's potential in thermal use originate from applications in aerospace engineering. NASA technical paper "A Design Handbook for Phase Change Thermal Control and Energy Storage Devices" (Humphries 1977, [4]) is considered to be one of the first comprehensive introductions to PCM thermal characteristics and

applications, along with PCM celled storage diffusion-controlled numerical results. The same topic remained active after decades of effort, especially when engineers successfully extended its applications into many other fields, for instance, waste heat capture [5], thermal management of Electronics and solar thermal engineering [1].

### ***1.1 Thermophysical Properties***

The performance of latent heat storage depends on a number of factors, the most obvious being the thermophysical properties of the PCM. As the effective component of paraffin, the properties of higher alkanes are well tabulated [4][6][7]. However, the blended alkanes performance is far more complicated in terms of melting profile, i.e., latent heat of fusion and melting range. For instance, Figure 1 illustrates the latent heat variation of a hexadecane-octadecane binary system with respect to mass fraction. To characterize the melting profile of a specific paraffin, differential scanning calorimetry is a frequently proposed tool. But to fully characterize the thermophysical properties, special apparatus are required for density, thermal conductivity, and viscosity measurement.

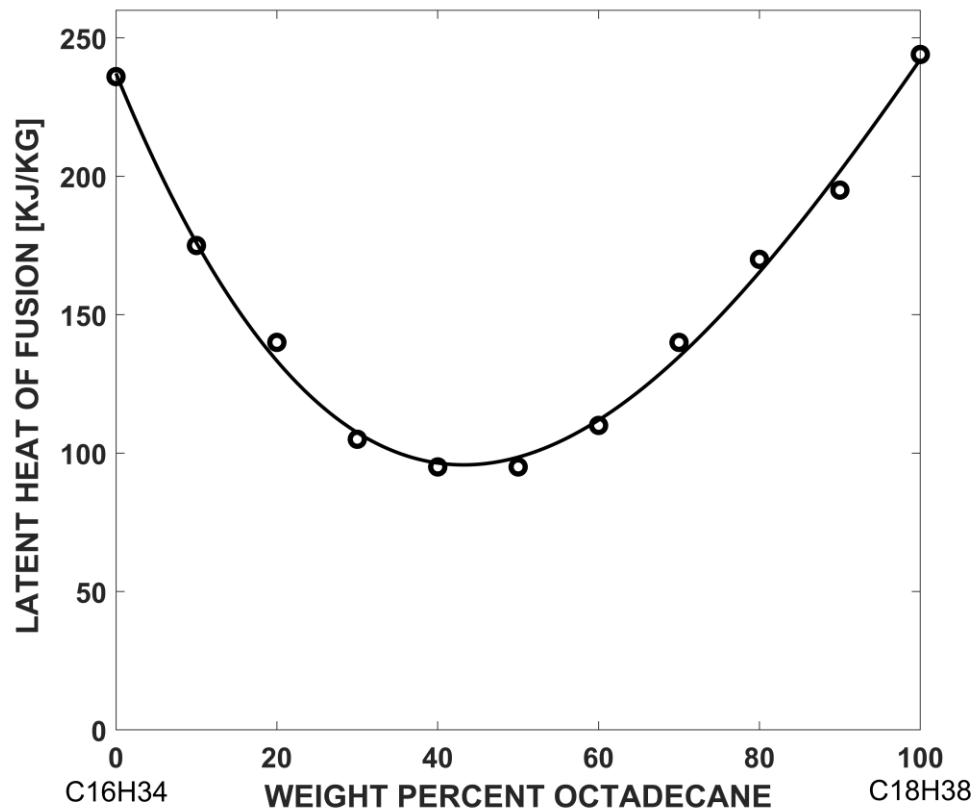


**Figure 1: Blending higher alkanes: Latent heat of fusion variation of hexadecane-octadecane binary system. Adapted from Humphries [4].**

Although paraffin generally performs well at latent heat and melting temperature, like many organic materials, it has a low thermal conductivity value. The high thermal resistance of paraffin prevents heat from rapid penetration, causing nonuniform temperature distribution and reducing the rate of heat storage. There are attempts of adding filler material with high conductivity into paraffin, which action could enhance the thermal conductivity in exchange of total heat capacity due to a reduced mass fraction of paraffin. Sari et al. [8] reported an 80% increase in overall

thermal conductivity by adding 2% mass fraction of expanded graphite, an encouraging result considering there is only a 2kJ/kg drop of latent heat from paraffin without any filler.

## **1.2 Modeling of Internal Convection Effect**

In general, convection is the dominant heat transfer process in liquid phase since for liquid paraffin,  $Pr \approx 80$ . The natural convection within the liquid phase is the origin of significant uncertainties between early diffusion-controlled numerical models and experimental data. Humphries [4] believes that the natural convection in liquid paraffin is the individual or combined effect of (a) buoyancy forces, (b) surface tension forces (the Marangoni effect) and (c) density change of solid-liquid transition. However, the Humphries' diffusion model, to serve space applications where the gravitational force is absent, is justified in neglecting buoyancy, but including the Marangoni flow induced convection [1]. In the environment of gravitational force near Earth's surface, on the other hand, the Marangoni effect is far less significant than buoyancy-driven convection. Numerical techniques regarding induced convection have been fully developed, but in phase change model, the effect has to be strictly restrained within the liquid phase while the solid phase remains diffusion controlled.

For an idealized Stefan type phase change problem where the solid-liquid transition occurred on an infinitesimally thin surface where properties discontinue across it, moving boundary approaches that track the fusion front have been developed

[9]. The scheme is to divide the PCM into two homogeneous domains, each representing either solid or liquid phase, then natural convection is solely taken into account within the liquid domain. The solid-liquid interface is defined as constant temperature boundary condition corresponding to the isothermal transition surface. The Stefan type assumption is valid for ice-water transition, where the PCM is a pure substance,

However, the fusion front of a mixture like paraffin is not a sharp edge: a mushy region exists and is filled by paraffin in the transition region where the change in density and thermal properties occurs. Voller et al. [10] first proposed a fixed grid convection-diffusion methodology that modeled the mushy zone as porous media, where the flow in the mushy region is governed by Darcy's law. Voller cleverly modified the momentum equation of fluid flow and the energy equation of enthalpy formulation by adding Darcy's law damping term, which describes the flow motion and heat transfer in the entire domain by one set of equations. This method, referred to as the enthalpy-porous formulation, has successfully become the most popular phase change numerical technique. Tan et al. [11] utilized the built-in enthalpy-porous phase change model of a commercial software to investigate radial phase change in a spherical capsule and showed good agreement on experiments. Ma [12] exerted the same software to enhance the performance of a tubular heat storage design by introducing cone shape fins, which reduced the melting time by 60% than no-fin design.

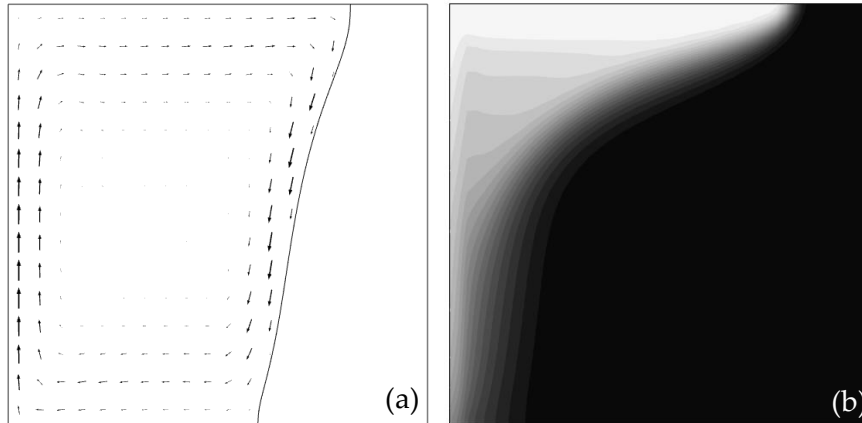


**Figure 2: (a) Typical phase distribution and natural convection velocity vector of a Stefan type melting problem, where the left edge is the hot surface, and the melting front moves rightward. Comparing with (b) solid, liquid, and mushy zone distribution generated by the enthalpy-porous numerical technique.**

To some extent, the density change of solid-liquid transition may affect the heat transfer. Taking paraffin as an example, a certain mass of paraffin that undergoes solid-liquid transition exhibits a 20% rise in volume. Therefore, during melting the liquid phase tends to flow away and make room for newly melted PCM, and during solidification the liquid PCM reversely fill the volume left by contraction [4]. This effect is reported to retard the phase transition [13] but in general is unimportant. However, the thermal expansion of PCM may cause leakage if PCM container not well designed [14]. The gravity also pulls the free moving solid phase into liquid, which usually changes the heat transfer process in tubular and spherical enclosures where the PCM is uniformly heated in radial directions. Bareiss et al. [15] and Moore et al. [16] provided analytical solutions of the unfixed solid PCM inside a horizontal tube and a sphere respectively, and both proved to be reasonable under certain conditions.



**Figure 3: Solid paraffin sinks in liquid. The mushy region is visible.**

### ***1.3 Active Storage Versus Passive Storage***

Many solar heat storage applications involve the use of heat transfer fluid, and for indoor heating purposes, water is the most important one. This type of configuration can be classified as active heat storage. Water is an effective heat transfer and sensible heat storage medium with low dynamic viscosity as well as high heat capacity. For a water-based latent heat storage system, the water temperature is raised by removing heat from collector during the daytime, and the heat stored in hot water is hereafter extracted into the heat storage medium. During nighttime, cold water is pumped through the latent heat storage again for heating purpose. The process is controllable and adjustable as different levels of heating may be desired. To accelerate the heat transfer process between water and PCM, the active latent heat storage often adopts

similar designs to heat exchangers, where the surface-to-volume ratio of PCM is increased. Typical designs include [1]: shell and tube heat exchanger, where water pipes are surrounded by PCM; packed bed, where lateral flow passes through PCM tube banks; and spherical capsules of PCM merged into the water flow. On the other hand, the rise in heat transfer rate is generally accompanied by the demands of higher pumping power to overcome the hydraulic loss.

A concise design of PCM involved in solar heating is utilizing integrated passive storage. This configuration was inspired by the Trombe wall and can be mounted either on the roof or the exterior wall of a building, minimize indoor space occupancy. The phrase “passive storage” referring to no working fluid requirement, results in theoretically higher energy efficiency by eliminating any pumping demand. With no pumping and piping, the overall system complexity is also reduced. However, the charging and discharging process of passive storage is spontaneous and cannot be manually controlled. As mentioned earlier, the low conductivity of organic PCM (paraffin) also limits the rate of heat storage. In his investigation of passive PCM storage Trombe wall, Christensen [17] emphasized that the effectiveness depends on the combination of the material itself and system design. The former includes the aforementioned highly conductive filler addition, or using alternative materials; the latter mainly focuses on the design of fins and cells. Hence, an investigation regarding melting pattern and design factors of passive storage is necessary to gain a deeper

insight into its applied potential. The future study in active heat storage may also benefit from the investigation of melting pattern in the passive storage, and vice versa.

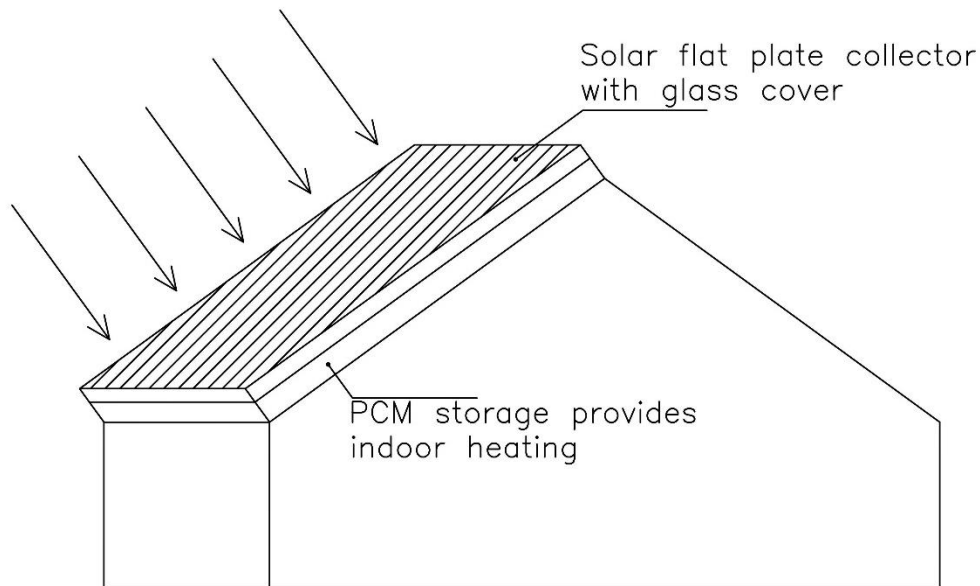


**Figure 4: The proposed geometry and application of a solar flat plate collector integrated storage.**

### ***1.4 Geometry of a Passive Storage***

In the early stage of the charging process of any latent heat storage, the heat transfer is diffusion controlled. To increase the efficiency of heat diffusion from the collector to the storage, every square inch of the solar flat plate collector should have a layer of PCM in its back. Thus, the thermal energy received can be greatly utilized: anywhere behind the collector, there is always a layer of PCM attached to it. A roof-mounted concept is illustrated in Figure 4.

### 1.4.1 Thickness of PCM Layer

Assuming the collector is uniformly heated up by solar energy, the heat diffusion process can be idealized to a 1D problem, where the heat flux is normal to the collector plane. By using energy conservation, the maximum thickness of PCM required can be roughly determined by the total amount of solar energy collected within one operation cycle. Due to heat loss, the maximum amount of energy collected is always less than the solar energy available,

$$Q < \int \left( \int I dA \right) dt \quad (1)$$

where the  $Q$  is the thermal energy stored, and  $I$  is the solar irradiance in unit  $W/m^2$ . The amount of heat stored in PCM is the sum of latent heat and sensible heat above ambient, which can be written as:

$$Q = \int_{T_{amb}}^T m c_p dT + ml \quad (2)$$

For an integrated collector-storage, the equation can be modified as heat absorbed per day on a unit area base. Assume constant specific heat capacity of the PCM,

$$Q'' = \rho b c_p (T - T_{amb}) + \rho b l \quad (3)$$

where  $Q''$  is the heat stored per unit area of collector,  $b$  is the thickness of PCM. Take

Durham, NC as an example, the average monthly global horizontal irradiance is

4.43kWh/m<sup>2</sup> per day [18], which is  $Q'' \leq 15.9MJ/m^2$  between sunrise and sunset. It

seems like a large value, but considering the high latent heat of the paraffin, the required thickness is relatively small. Assume the amount of heat is just enough to raise and melt

a paraffin by 50°C from an ambient temperature 20°C, and plug in the typical value of paraffin properties where  $\rho = 800\text{kg}/\text{m}^3$ ,  $c_p = 2600\text{J}/(\text{kg} \cdot \text{K})$  and  $l = 200,000\text{J}/\text{kg}$ ; the thickness obtained is then  $b \leq 0.07\text{m}$ . That is, a collector-storage with 3-inch thickness of homogeneous paraffin is more than sufficient to store the solar energy collected in one day.

However, such a geometry creates a high surface-to-volume ratio; the effect of buoyancy-induced natural convection is suppressed due to viscous loss along the wall. The time-dependent efficiency of this thin layer design remains unknown, and it will be meaningless if the PCM layer cannot be melted in the daily sunshine hours. The heat transfer of the thin geometry should be thoroughly investigated before some enhancement measurement is applied.

### **1.5 A Scope of Present Work**

This study focuses on the heat and mass transfer process of the integration of solar energy collection and storage. Firstly, a numerical approach using the enthalpy-porous formulation serves as the starting point of the study, and the calculation is explained in section 3. Contours are provided to illustrate how the buoyancy-induced convection affects the melting front. The general performances of the simplified two-dimensional model are predicted by transient plots. Then, a test rig was designed and built to experiment on the actual feasibility and performance of a demonstration collector (from now on referred to as 'collector'). The experimental apparatus is depicted

in section 4. The phase change process of the paraffin inside the collector is monitored by thermocouple arrays, while the solid-liquid boundary progression along the back plate is recorded in sequence photography.

In most of the latitude that suits solar engineering, the collectors are often oriented to a fixed angle to maximize the incoming solar energy without tracking effort. In response to the potential inclination effect, two sets of numerical studies and experiments were carried out. In numerical cases, the inclination is achieved by input of the x and y components of the body force (gravity). Several hypotheses were also made based on these numerical results. In experiments, the entire test rig is pivoted to provide the inclination without affecting the incoming radiation intensity. By comparing numerical and experimental results, important features of the performance of a solar flat plate collector with integrated heat storage are characterized.

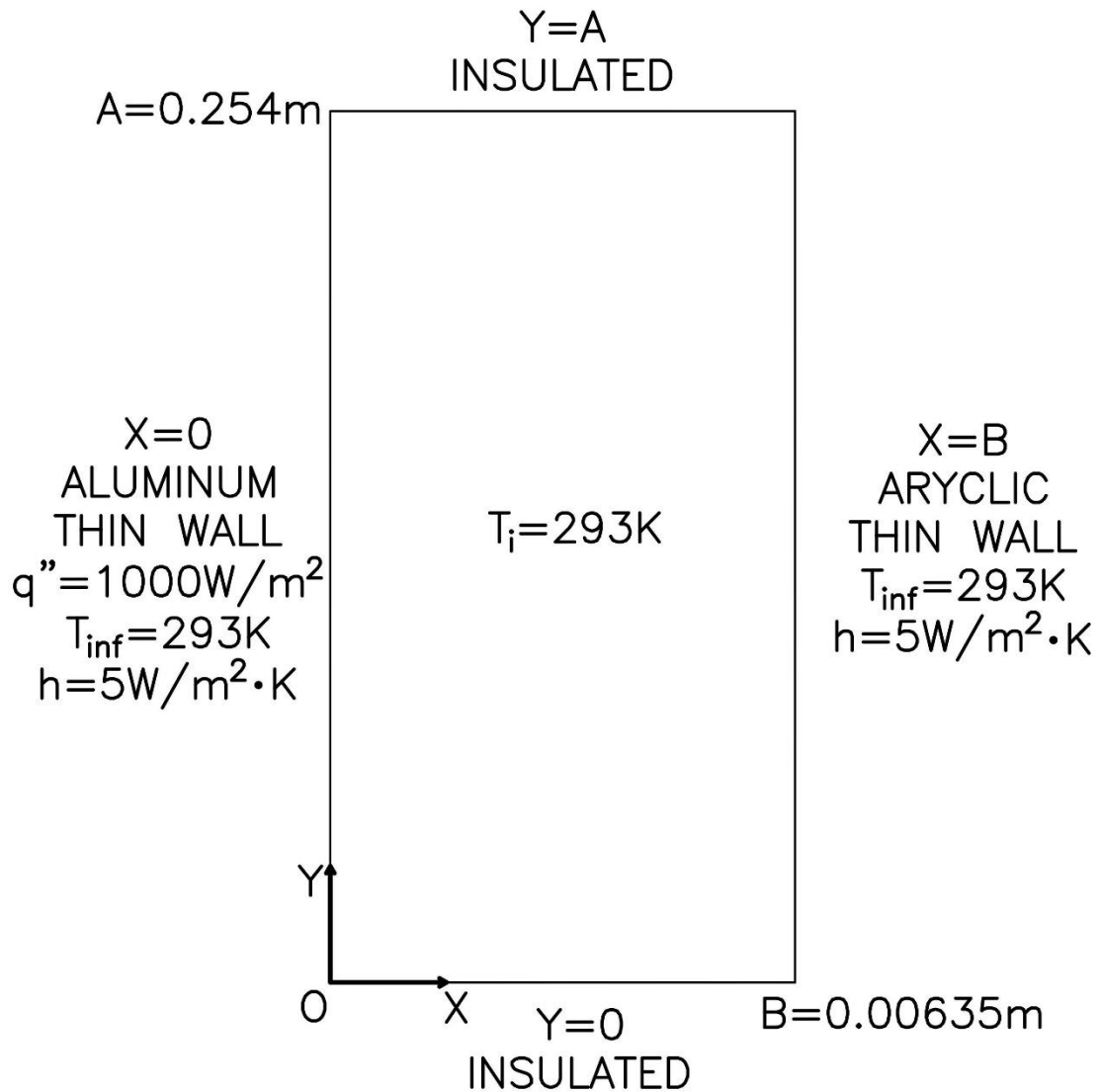
## 2. Numerical Analysis

The objective of using a numerical approach is to deepen the understanding of the mass and heat transfer pattern, as well as time responses associated with the geometry. If the calculations showed any unreasonable melting performance, the attempt to combine the solar heat collection and storage needs reevaluation. Fortunately, the calculation results are encouraging.

The computational domain with boundary and initial conditions are described in section 2.1. In section 2.2 the governing equations of enthalpy-porous formulation, especially the momentum and energy source terms, are explained. The solver setup and material properties are given in section 2.3. Contours and plots are provided in section 2.4 with interpretations.

### ***2.1 Computational Domain***

To investigate the convection effect and melting time, the heat and mass transfer in a two-dimensional domain is numerically solved. The geometry and boundary conditions are illustrated in Figure 5. Note for better view x-direction is enlarged. The domain is a  $0.00635\text{m} \times 0.254\text{m}$  ( $0.25'' \times 10''$ ) rectangle with a 1:40 height to width ratio.



DIMENSIONS NOT TO SCALE  
 X-DIRECTION ENLARGED

Figure 5: The dimensions, boundary conditions, and the initial condition of the computational domain.

The reason for using a relatively complicated boundary condition is to model the reality as much as possible. In many phase change numerical studies, the isothermal boundary condition is a reasonable assumption for pipe heating [19][20]. The insulation, on the other hand, is more close to a constant heat flux boundary condition, but the error due to external convection loss grows over time when the surface temperature builds up. To compensate for the external convection loss, the convection boundary condition is applied with a uniform but not constant surface temperature. The freestream temperature is set to 20°C(293K) and the constant convective heat transfer coefficient is 5W/(m<sup>2</sup>·K). The value was an arbitrary choice until it was shown to be reasonable. Heat loss analysis is given in the following subsection.

### 2.1.1 Heat Loss Coefficient

The external natural convection has been fully correlated for both vertical walls and inclined walls. These correlations include the relation of average Nusselt number to Grashof number, Prandtl number, and Rayleigh number. Assume isothermal plate with wall temperature 60°C(333K) has been reached, these dimensionless numbers are calculated based on air at film temperature  $\frac{T_w - T_\infty}{2} = 313K$  ( $\alpha = 2.4 \times 10^{-6} \frac{m^2}{s}$ ,  $\beta = 3.2 \times 10^{-3}/K$ ,  $\nu = 1.7 \times 10^{-6} m^2/s$ ,  $Pr = 0.71$ ) with plate height  $a = 0.254m$ . To find the appropriate value of the convective heat transfer coefficient, multiple correlations were used for comparison. Using the isothermal plate assumption, the correlations and the results based on specific temperature differences are given in Table 1. Note The

Churchill and Chu's equation of inclined wall does not discriminate between heat loss from hot surface facing upwards and downwards, but the predictions by Fujii and Imura's equations showed small difference.

The correlation results vary in a small range near  $5W/m \cdot K$ . It is worth noting that the dimensionless numbers and coefficient are more or less temperature-dependent, while the analysis is based on  $60^{\circ}\text{C}$  isothermal assumption. Constant coefficients underestimate or overestimate the heat loss in transient and locally, but the error should be small.

**Table 1: The derived dimensionless numbers and convective heat transfer coefficient value by external natural convection correlations [21]**

Vertical wall				
Correlation	Gr	Ra	$\overline{Nu}$	$\frac{h}{(W/m^2 \cdot K)}$
Churchill and Chu [22] $\overline{Nu} = \left\{ 0.825 + \frac{0.387Ra^{\frac{1}{6}}}{[1 + (0.492/Pr)^{9/16}]^{8/27}} \right\}$	$7.21 \times 10^7$	$5.12 \times 10^7$	50.1	5.39
$\overline{Nu} = 0.68 + \frac{0.67Ra^{1/4}}{[1 + (0.492/Pr)^{9/16}]^{4/9}}$			44.2	4.76

Inclined wall at an angle orientation relative to the horizontal  $\theta = 60^\circ$

Correlation	Gr	Ra	$\overline{Nu}$	$\frac{h}{(W/m^2 \cdot K)}$
Churchill and Chu [22] $\overline{Nu} = \left\{ 0.825 + \frac{0.387Ra^{\frac{1}{6}}}{[1 + (0.492/Pr)^{9/16}]^{8/27}} \right\}$	$6.24 \times 10^7$	$3.63 \times 10^7$	45.3	4.88
Fujii and Imura [23] $\overline{Nu} = 0.16Ra^{\frac{1}{3}} \text{ (Facing upwards)}$			53.0	5.71
Fujii and Imura $\overline{Nu} = 0.56Ra^{\frac{1}{4}} \text{ (Facing downwards)}$			43.5	4.68

## 2.2 Equations

The 2D continuity, momentum, and energy equations of the enthalpy-porous formulation are given below [12][24],

### Continuity equation

$$\frac{\partial \rho}{\partial t} + \frac{\partial(\rho u)}{\partial x} + \frac{\partial(\rho v)}{\partial y} = 0 \quad (4)$$

### Momentum equation

$$\rho \left( \frac{\partial u}{\partial t} + u \frac{\partial u}{\partial x} + v \frac{\partial u}{\partial y} \right) = \mu \left( \frac{\partial^2 u}{\partial x^2} + \frac{\partial^2 u}{\partial y^2} \right) - \frac{\partial p}{\partial x} + S_u \quad (5)$$

$$\rho \left( \frac{\partial v}{\partial t} + u \frac{\partial v}{\partial x} + v \frac{\partial v}{\partial y} \right) = \mu \left( \frac{\partial^2 v}{\partial x^2} + \frac{\partial^2 v}{\partial y^2} \right) - \frac{\partial p}{\partial y} + S_v \quad (6)$$

where  $S_u$  and  $S_v$  are the source term, or Darcy's law damping term on x and y direction respectively:

$$S_u = \frac{(1 - \lambda)^2}{(\lambda^3 + \varepsilon)} A_{\text{mush}} u + \rho_{\text{ref}} g_x (t - t_{\text{ref}}) \quad (7)$$

$$S_v = \frac{(1 - \lambda)^2}{(\lambda^3 + \varepsilon)} A_{\text{mush}} v + \rho_{\text{ref}} g_y (t - t_{\text{ref}}) \quad (8)$$

$\varepsilon$  is assigned a positive constant of less than 0.001 to avoid the singularity. Mushy zone constant  $A_{\text{mush}}$  is a damping parameter and often between  $10^4$ - $10^7$ . The constant only exists numerically and is reported to affect the melting rate near liquidous temperature [36]. The porosity  $\lambda$  is the key parameter in determining the phase and is a function of temperature only. The value of  $\lambda$  is equal to 0 in solid state and 1 in liquid state, which is also assumed to be linear between solidus temperature and liquidous temperature:

$$\lambda = \begin{cases} 0 & (T < T_S) \\ 1 & (T > T_L) \\ \frac{T - T_S}{T_L - T_S} & (T_S < T < T_L) \end{cases} \quad (9)$$

### Energy equation

$$\rho \left( \frac{\partial h_{\text{tot}}}{\partial t} + u \frac{\partial h_{\text{tot}}}{\partial x} + v \frac{\partial h_{\text{tot}}}{\partial y} \right) = \frac{k}{C_p} \left( \frac{\partial^2 h_{\text{tot}}}{\partial x^2} + \frac{\partial^2 h_{\text{tot}}}{\partial y^2} \right) + S_h \quad (10)$$

the energy source term is

$$S_h = \frac{\rho}{C_p} + \frac{\partial(\lambda l)}{\partial t} \quad (11)$$

where  $h_{\text{tot}}$  is the total enthalpy of PCM, which is the summation of sensible heat and latent heat:

$$h_{\text{tot}} = h_{\text{sen}} + \lambda l \quad (12)$$

$$h_{\text{sen}} = h_{\text{sen,ref}} + \int_{T_{\text{ref}}}^T c_p dT \quad (13)$$

The formulation is based on the following assumptions:

- (1) Thermophysical properties in the solid and liquid phase are isotropic and homogeneous
- (2) Buoyancy force in the liquid phase is determined by Boussinesq approximation.

### 2.3 Solver setup

A finite-volume commercial software, ANSYS® Academic Research Fluent, Release 19.0, has been employed to solve the unsteady enthalpy-porous formulation with gravity body force. The properties of n-tetracosane ( $nC_{24}H_{50}$ ) with 49-52°C melting range have been used in the computation, given in Table 2. Although n-tetracosane is not good modeling of paraffin with a similar melting point, since most paraffin products in the market are not characterized, a compromise must be made.

**Table 2:** Thermophysical properties of n-tetracosane [25][26][27][28][29]

Liquid Density at 52°C ( $kg/m^3$ )	Thermal Conductivity ( $W/m\cdot K$ )	Heat Capacity ( $J/kg\cdot K$ )	Dynamic Viscosity ( $Pa\cdot s$ )	Latent Heat ( $kJ/kg$ )	Solidus Temperature (K)	Liquidus Temperature (K)
778	0.15	3000	0.004	260	322 (49°C)	325 (52°C)

The solver setup is given in Table 3. Unspecified setting remains default. To meet the criteria of convergence, the combination of mesh size and time step is crucial. The domain is uniformly divided by 2560 square cells, each has  $6.3\times 10^{-7}m^2$  area, and 0.1s is the maximum allowing time step to converge. For a melting process, a good convergence might be obtained in the diffusion stage, but the performance usually deteriorates when the liquid fraction and velocity magnitudes increase. Therefore, in troubleshooting an initial temperature close to the solidus point should be used. This will uncover any convergence problem without a long waiting.

**Table 3: Phase change specified solver setup**

<b>Solver Setup</b>	<b>Input or Selection</b>
Meshy zone constant	10 <sup>5</sup>
Pressure-velocity coupling scheme	SIMPLE
Spatial Discretization – Pressure	PRESTO!
Momentum scheme	Second-order upwind
Energy scheme	Second-order upwind
Residual – continuity	1e-4
Residual – x velocity	1e-6
Residual – y velocity	1e-6
Residual - energy	1e-9
Max iterations	100
Time step	0.1s

## **2.4 Results**

The solutions of numerical study are mostly given in contours and plots.

Contours provide a straightforward view of distribution over the entire domain, such as temperature and a liquid fraction, which tells the heat transfer pattern immediately. The plots are more intuitive in illustrating the trend of a specific value over time.

Something beyond expectation is that for both vertical and inclined angular orientations, the results are almost identical in phase and temperature distribution. Differences can be noticed in later time steps but are very small. At first, the calculation on 60° inclination case was suspected of having the wrong body force vector input, but the pressure contour in liquid phase proved no mistake was made in the setup stage. This means numerically, the inclination has no visible effect on the mass and heat transfer. Since the differences between the two angular orientations are too small to identify, only one set of results (vertical) is displayed

### **2.4.1 Phase Distribution**

The phase distribution in the sequence is given in Figure 6 and Figure 7 in the following two pages. The time interval between each contour is 10 minutes, starting at  $t = 20 \text{ min}$ . In each contour, the three lines from left to right are of  $\lambda = 0.75, \lambda = 0.5$  and  $\lambda = 0.25$ , i.e., 75%, 50% and 25% of the mass fraction is liquid. A similar shape distribution of the liquid phase in the rectangle domain is also observed in many other

numerical investigations [12][24][30], a strong evidence of the existence of convection effect.

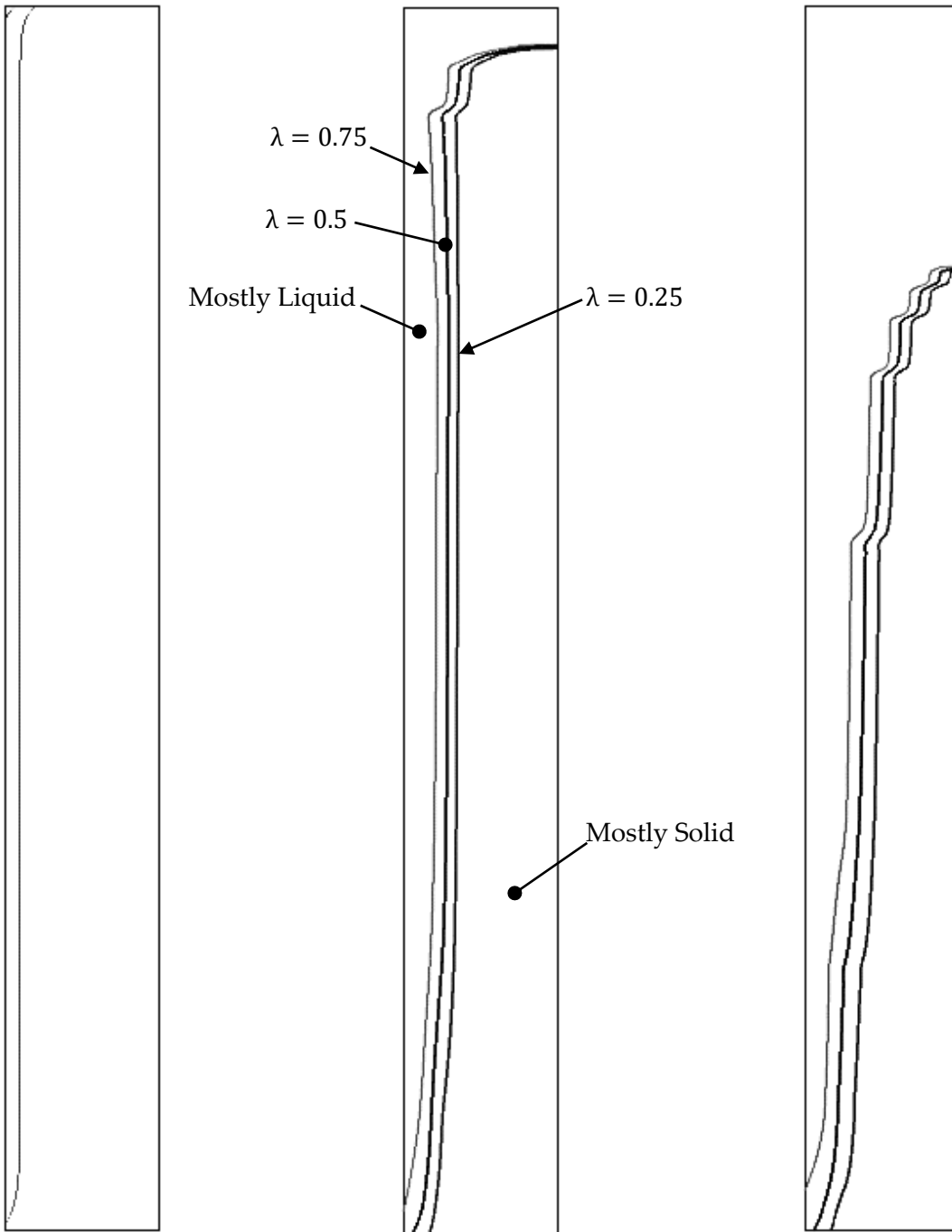


**Figure 6: From left to right, mass fraction contour at  $t = 10\text{min}$ ,  $t = 20\text{min}$  and  $t = 30\text{min}$ . Contour enlarged in x-direction by a factor of 5.**

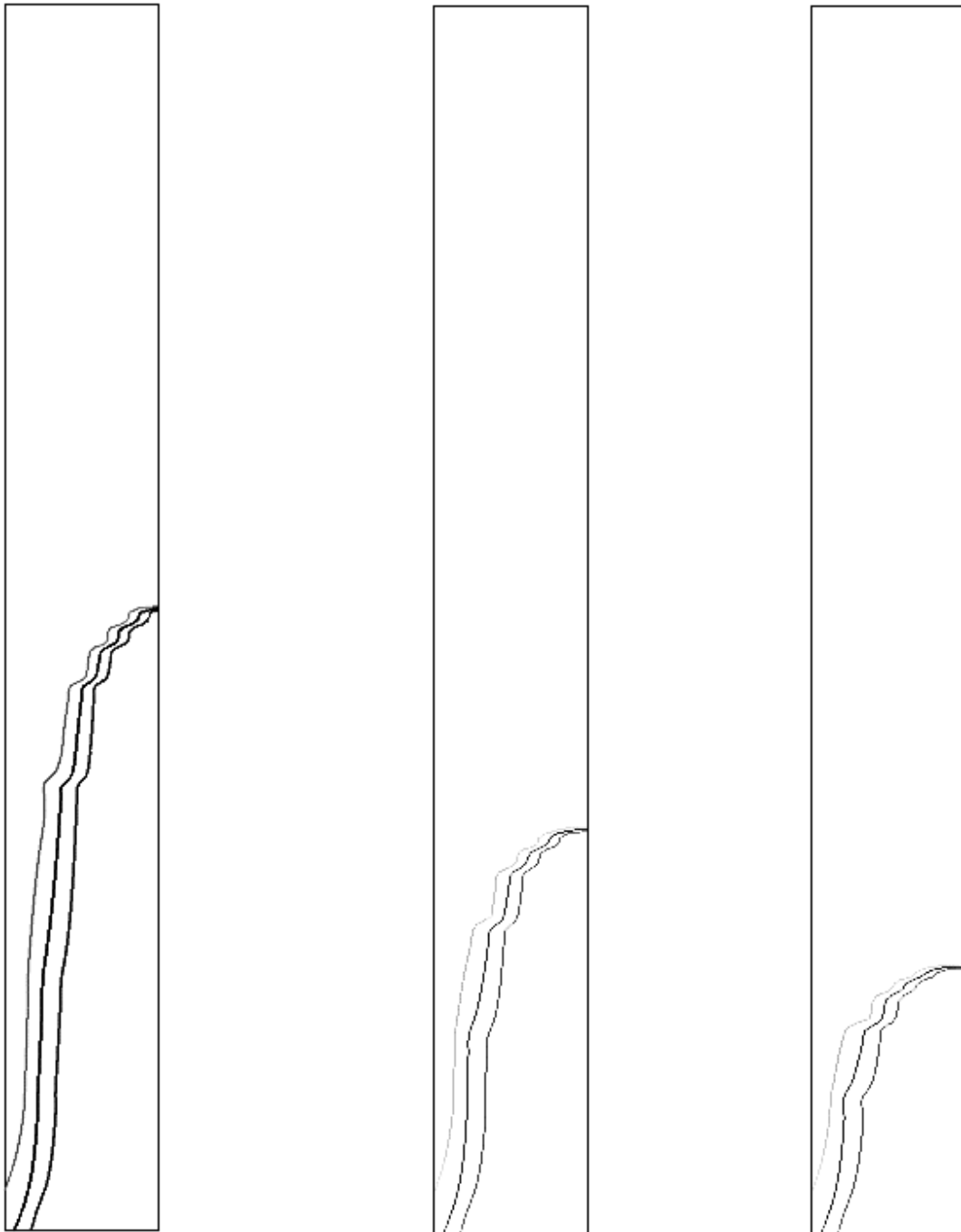


**Figure 7: From left to right, mass fraction contour at  $t = 40\text{min}$ ,  $t = 50\text{min}$  and  $t = 60\text{min}$ . Contour enlarged in x-direction by a factor of 5.**

## 2.4.2 Liquid Fraction

From phase contours, the melting of paraffin seems to accelerate and then decelerate as time progresses. This can be verified by the transient plot of liquid fraction in the Figure 8 below.

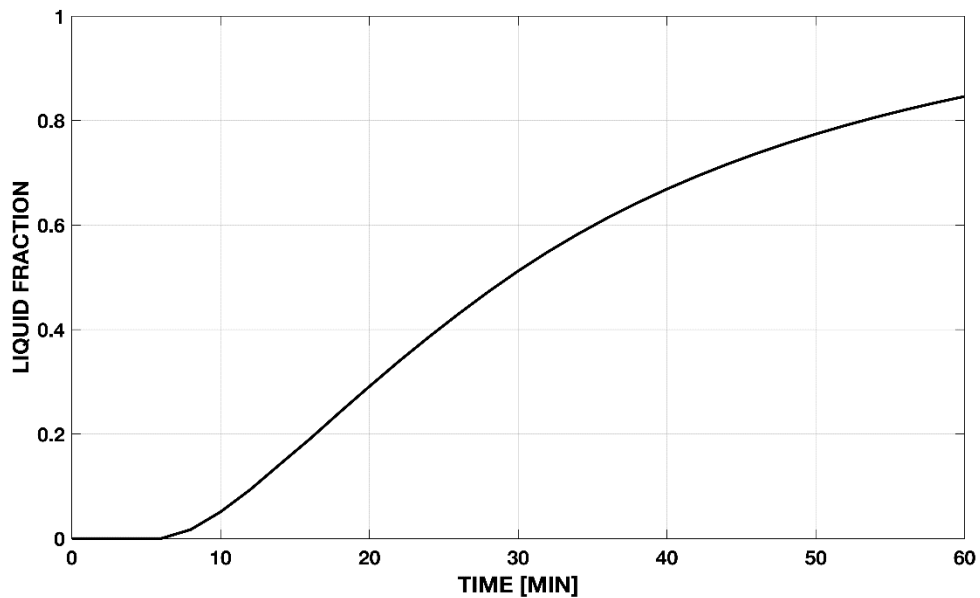


**Figure 8: The calculated liquid fraction.**

From the fraction variation, the liquid phase first appeared at  $t = 6$  min, shortly the melting process reached its maximum speed in between  $t = 10$ min and  $t = 20$ min, before slowing.

### 2.4.3 Temperature and Velocity Distribution

In comparing the isothermal and velocity contours, it is evident that the thermal boundary layer is thicker than the momentum boundary layer, which is reasonable, recalling the Prandtl number of n-tetracosane is of order 100.

The temperature contours also showed an apparent stratified structure, which corresponds to the buoyancy force in the liquid phase. In the solid region at the right corner of temperature contours, the temperature gradient is small due to the low conductivity. Near the top of the solid-liquid boundary there is the mixing of the upward and downward stream, in which region the maximum velocity magnitude around  $1.3 \times 10^{-3} m/s$  is reached.

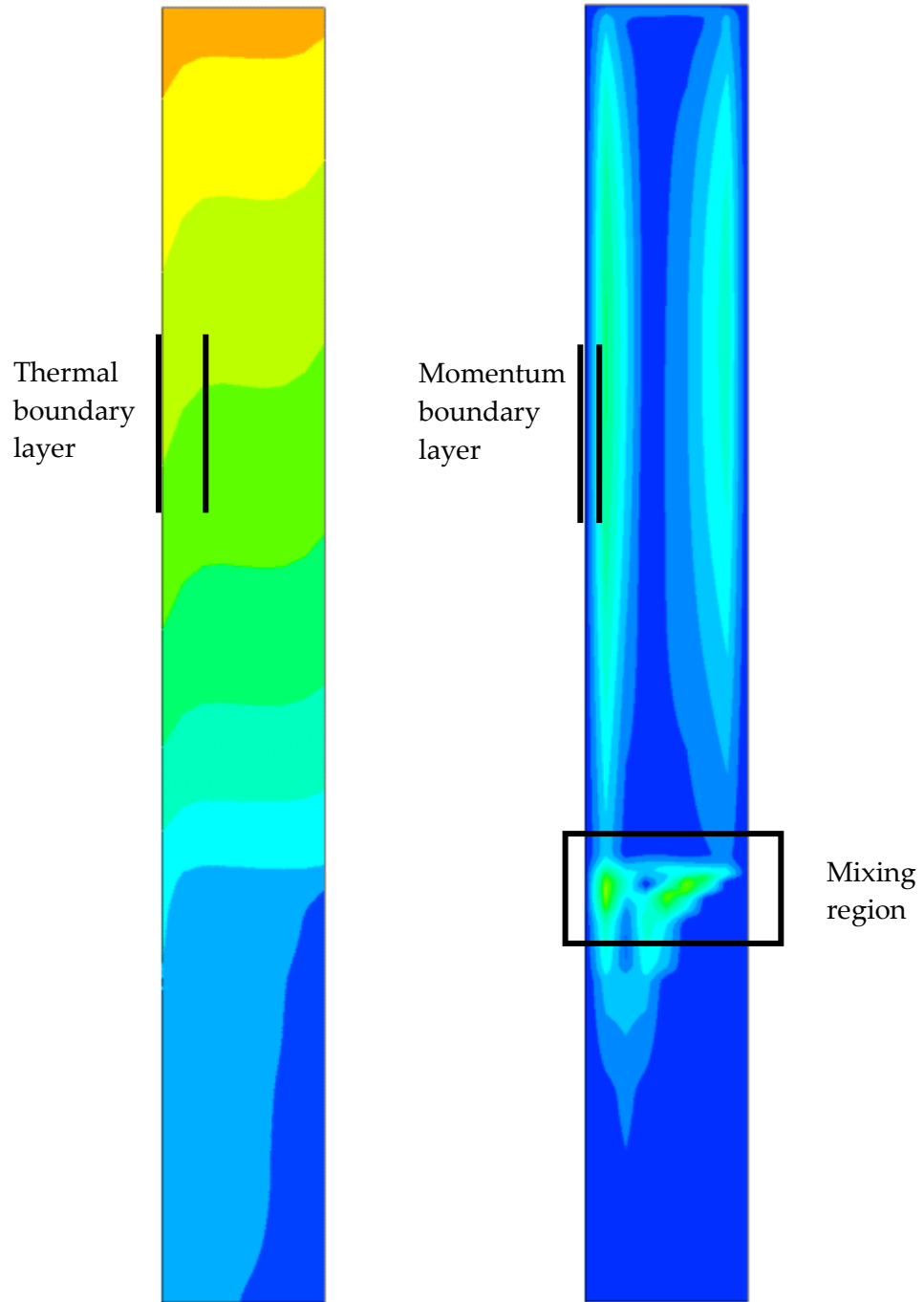
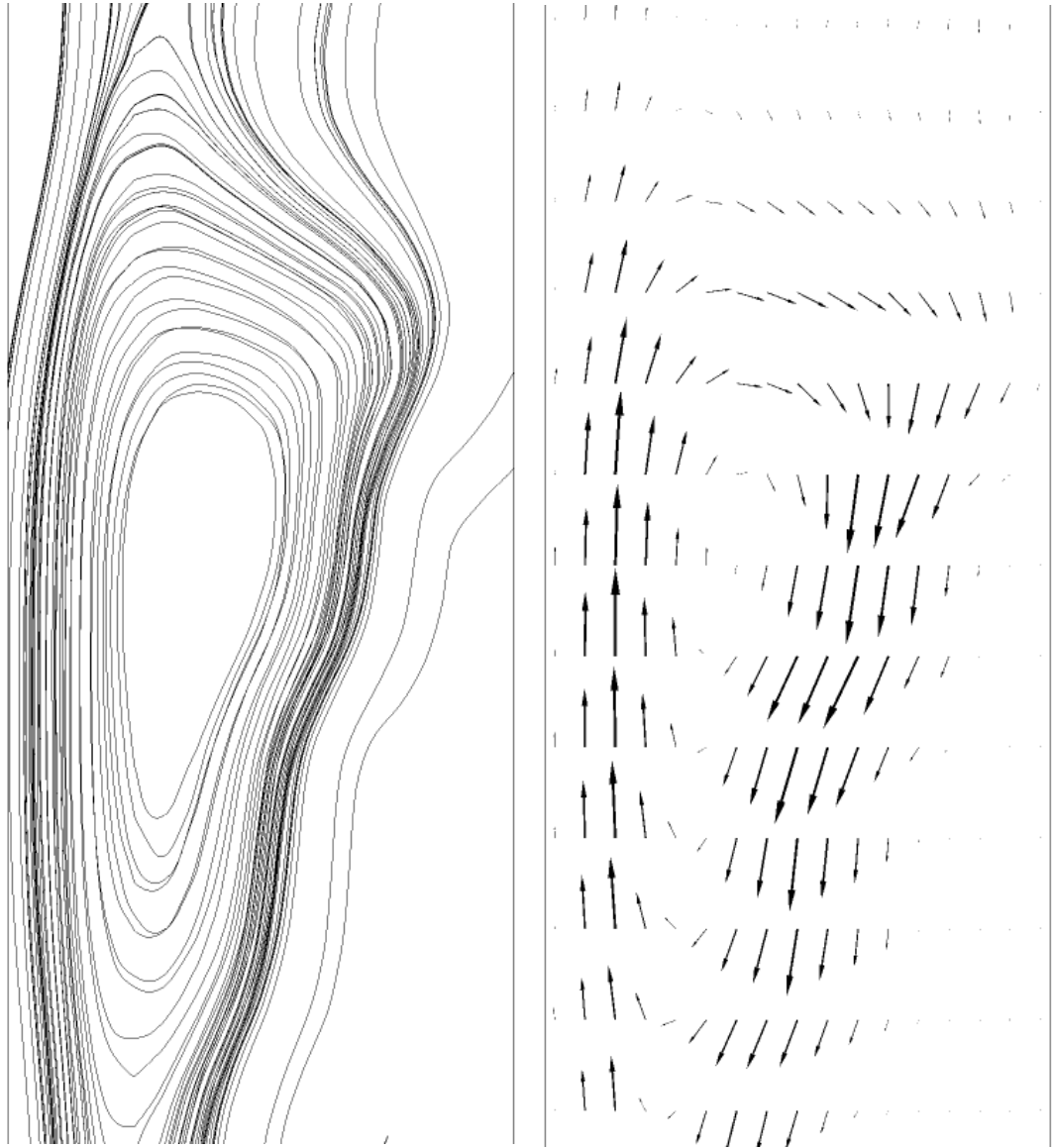


Figure 9: Isothermal and velocity contour at  $t = 50$  min (Vertical). Contours enlarged in x-direction by a factor of 5.



**Figure 10: Streamlines and the velocity vectors in the mixing region.**

#### **2.4.4 Summary of Numerical Findings**

The calculations of the enthalpy-porous formulation in the two-dimensional geometry considered for experiments indicates a melting pattern consistent with other calculated results. This pattern can be found in a two-dimensional planar result with extended x dimension by Zou, et al. [24], and an axisymmetric case by Ma [12], as well as an axisymmetric case by Lorente, et al. [30] using a different finite element software.

Mass fraction contours show an initial thin mushy layer along the plate from top to bottom by diffusion, then the PCM at the top rapidly proceeding in x direction where the convection effect in the mushy zone is reshaping the solid-liquid progression. As the liquid fraction increases and the convection effects become significant, a liquid layer is established near the front plate, with a liquid section spanning the total thickness at the top of the domain. At that moment and after, the convection has dominated the mass and heat transfer process, and the melting proceeds largely downwards. Speed of the melting increases initially but decreases toward the end of melting. Although the cross-section is too thin to view in practice, the progression of solid-liquid boundary near the back plate leaves an evolution process that could be visibly validated.

Eighty percent liquid fraction is predicted within 60 minutes, indicating that the size and configuration of the PCM mass is reasonable for demonstrating the feasibility of an integrated collector through experiment.

### **3. Experiment Setup and Results**

A technical grade of paraffin obtained from MilliporeSigma has been chosen as sample PCM, the labeled melting range in between 51-53°C. The product is in small white pellets at room temperature, and shows an excellent transparency and fluidness in the liquid phase. The sample undergoes several DSC test cycles before testing in the collector.

#### ***3.1 Material Properties from Differential Scanning Calorimetry***

A small pastille of sample paraffin weight 37.7mg has been heated up inside the 99% purity nitrogen atmosphere of SDT Q600 DSC/TGA instrument with 3°C/min heating rate. The relevance of DSC curve shapes on the heating rate is reported by Anghel et al.[31] and small heating rate is recommended to reduce error [32]. Transient heat flux and the corresponding temperature are automatically collected at sampling rate once per second.

The plot of transient heat flux versus temperature given in Figure 10 shows two heat absorption peaks covering a wide temperature range. This phenomenon proves the existence of non-isothermal phase transition, which means Stephan phase change analysis is inappropriate. Similar curve shape can be found in [31], where the number of absorption peaks may vary depending on different paraffin. The first peak is considered as the solid-solid transition, where some early structural change among n-folded alkane chains, starting just 10 degrees above ambient. At 45°C, although the paraffin has been

through its first absorption peak, it is still in solid state with no mushiness. The solid-liquid phase change occurs at a temperature corresponding to the steepest slope on the heat flux curve between 49°C and 56°C.

To obtain heat of transition and latent heat of fusion, peak values are integrated respectively on an arbitrarily selected baseline between a peak on and off point. However, the transient heat flux plot is incomplete where the sensible heat curve is below the instrument's operating temperature. Without knowing the actual baseline, the peak integration value illustrated in Figure 10 is considered to be smaller than the actual value.

The DSC results showed a large difference in phase change characteristics between the materials used in numerical analysis and experiments. The paraffin sample used in experiments has a long phase transition process covering a 20°C temperature interval, while for n-tetracosane, this interval is only around 3°C.

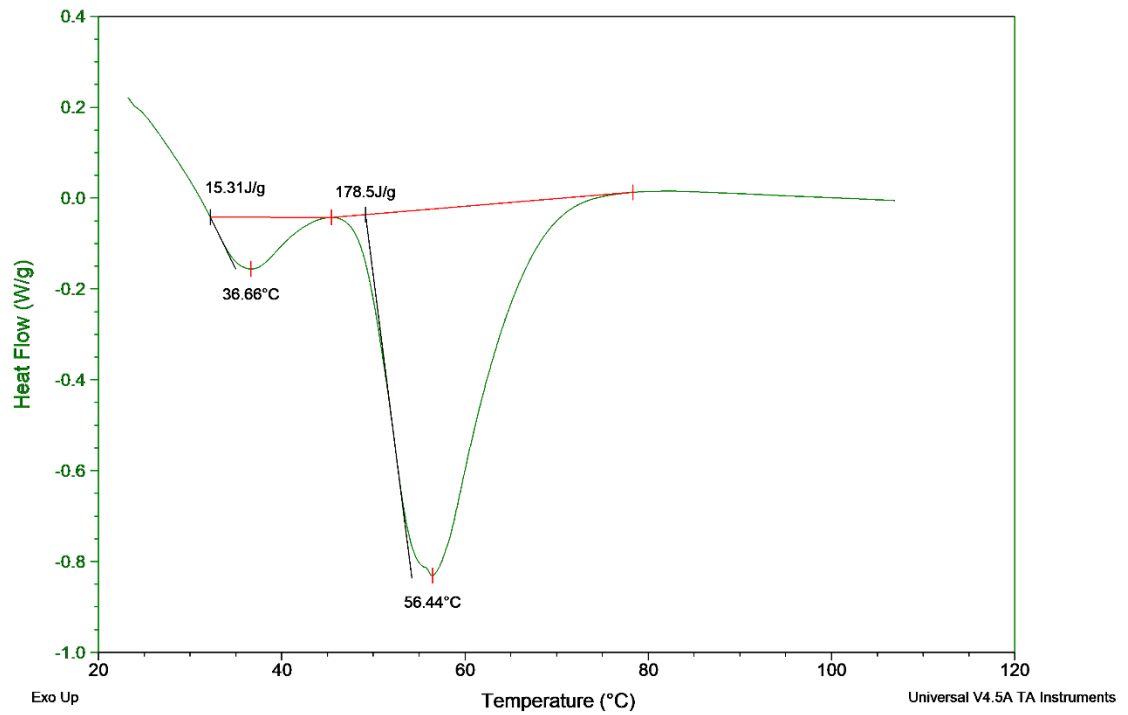
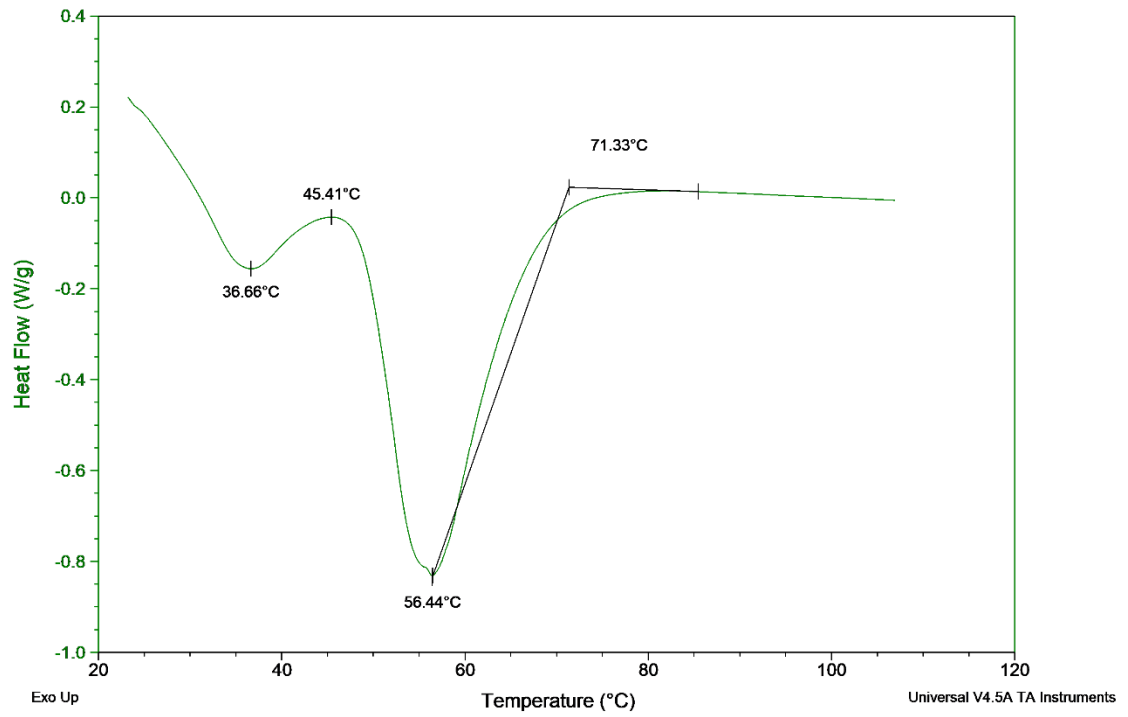
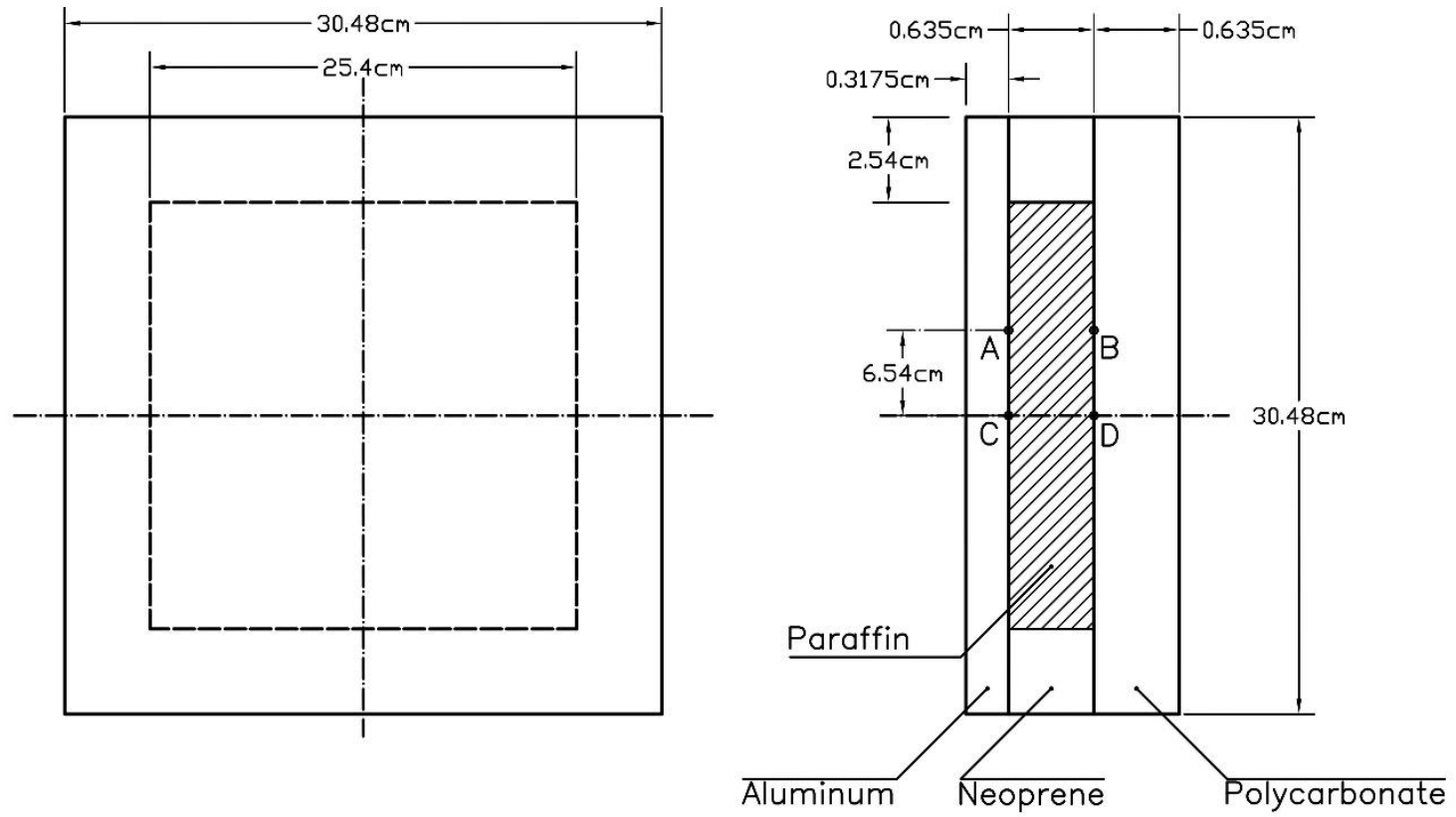


Figure 11: DSC curves.

### **3.2 Integrated Phase Change Storage Demonstration Collector**

The collector is a multi-layer sandwiched structure illustrated in the schematic of Figure 11. Note schematic dimensions are not to scale. The square aluminum plate is responsible for collecting and transferring the thermal energy to paraffin through conduction. The surface toward radiation is painted black for better surface emissivity, which is approximately determined to be  $0.90 < \varepsilon < 0.95$  by an infrared thermometer. The transparent acrylic sheet in the back allows visualization of the interior. Neoprene rubber has been adhered around the edge between the front and back sheets as a spacer and gasket, holding the paraffin in between. Two 12.7cm-long aluminum round tubes having 0.457cm ID and 0.635cm OD, although not illustrated in the schematic, are inserted at the top edge, through which the 0.4-liter liquid paraffin is injected by syringe. The round tube also acts as a channel connecting inside and outside of the enclosure, allowing paraffin to expand during phase transition.

An array of four thermocouples are embedded in the paraffin, two (point A & C) attached to the front plate and two (point B & D) to the back plate. The thermocouples are fixed in position by adhesive tape, but the probe is exposed in paraffin. All four thermocouples were calibrated and showed good consistency. To indicate the relative position of the fusion front near the acrylic sheet, a paper length scale is affixed to the internal surface, and a metal tape is attached at the symmetric position.



DIMENSIONS NOT TO SCALE

Figure 12: The schematic of the reduced scale solar flat plate collector integrated storage demonstration module. Left: front view. Right: Cross-section

### **3.3 Rig Tests**

The collector was mounted in a frame that also supported the lamps for insolation input. The purpose of building the frame is to provide discrete variable inclination for the collector, while keeping the radiation normal to the front plate of the collector. Halogen lamps have been used to model the solar radiation, explained in subsection 3.3.1.

Two identical collectors were built and tested. The paraffin in each collector has been through a complete melting-solidification cycle before real tests, in which process the air bubbles sealed in the paraffin is removed. Each collector was clamped on the test rig and melting cycles were run in vertical and 60° inclination. In total four cycles were recorded.

#### **3.3.1 Radiation Heat Source**

To demonstrate its feasibility, the collector is supposed to be tested under sun beam. However, the actual solar irradiance intensity varies depending on multiple aspects. Even though the sun position can be tracked at the cost of great effort, weather influence is inevitable. As an alternative solution, the artificial radiation source that simulates real solar irradiance is often adopted in laboratory environments [33].

Tungsten-halogen work lamps are compact, capable of delivery high radiation intensity at a low cost. But the spectrum has double the intensity near infrared compared with actual sunlight. The spectrum difference has been reported to cause abnormal

temperature rise in glasses [37], instead Dysprosium lamps with improved spectrum similarity are recommended [34]. In this experiment, no glass part has been used. The emissivity of the painted receiver plate is assumed to have no spectrum dependence.

The radiation is also projected from a point source, which results in a poor uniformity. Although the uniformity can be improved by extending the distance between the source and the target, the intensity will decrease. Hence, the test rig equipped with four 500W halogen lamps, and by overlapping, the lamp sets generate a radiation intensity  $I = 1050 \pm 50 \text{ W/m}^2$  at a fixed distance of 90cm. The radiation intensity is measured by an Eppley Laboratory standard precision pyranometer, and the value is close to the high end of the possible solar radiation in the earth temperate zone.

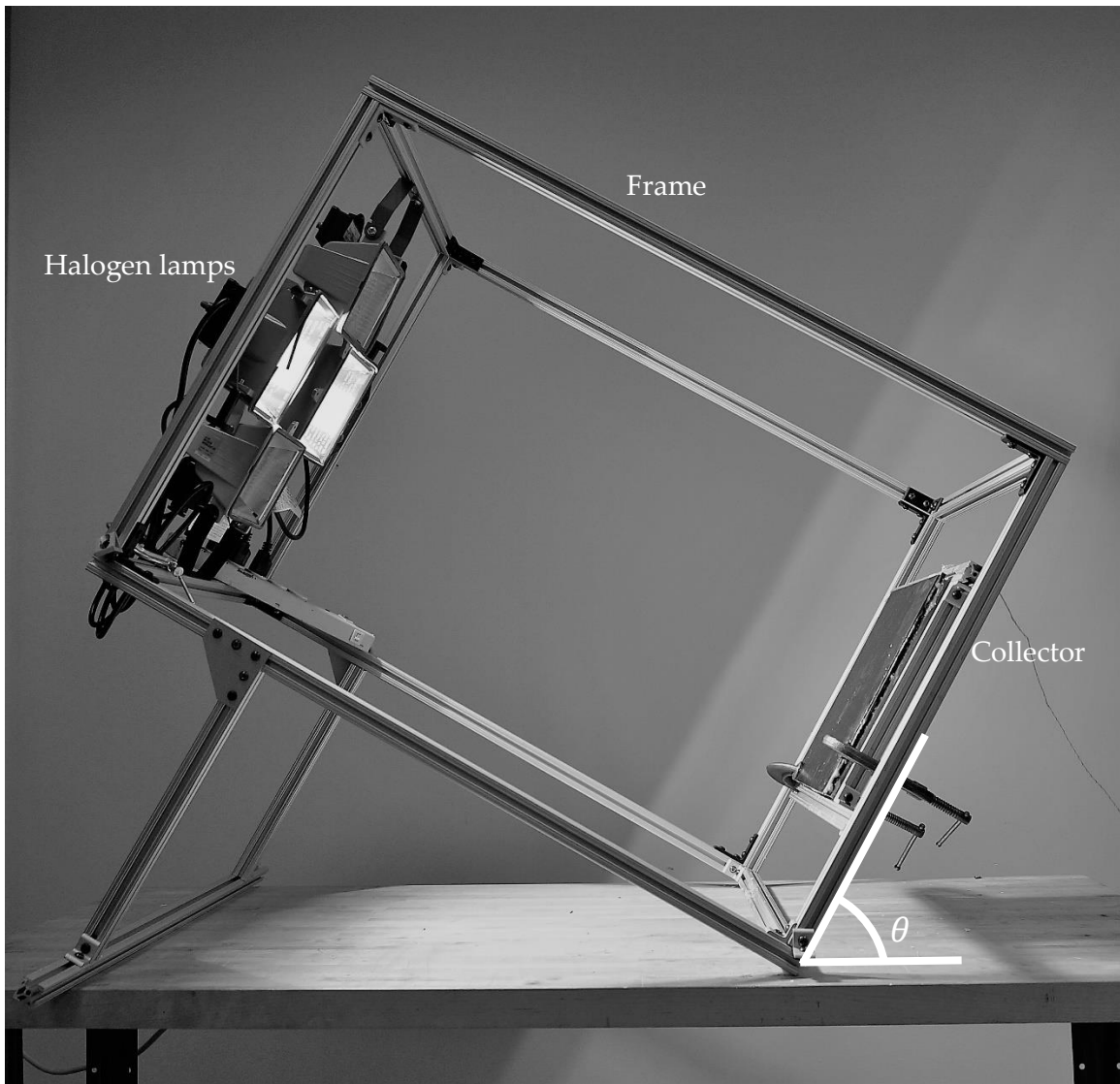


**Figure 13: The tilted test rig. The demonstration collector on the right is clamped and inclined. The lamps at a fixed distance provide light beam normal to the front plate.**

### **3.4 Experiment Results**

Photographs of the melting are shown in Figure 14 to Figure 24. The photographs of collector #1 were taken in less contrast, therefore only photographs of collector #2 were included. Evolutions of solid-liquid boundary in both angular orientations are summarized in Figure 25 and Figure 26. For both collectors, the measured temperatures are given in Figure 27 and Figure 28.

#### **3.4.1 Collector Vertical**

The solid-liquid boundary appeared around  $t = 40$  min. Then the sequence of photographs were taken with 10 minutes' interval. The expansion of liquid section near the top follows the trend of calculated results. Although the solid-liquid boundary bends after a while, the progression is generally downward.



**Figure 14: Solid-liquid boundary at  $t = 40$  min (Collector #2, vertical). Small amount of liquid phase appeared at the top.**



**Figure 15: Solid-liquid boundary at  $t = 50$  min (Collector #2, vertical).**

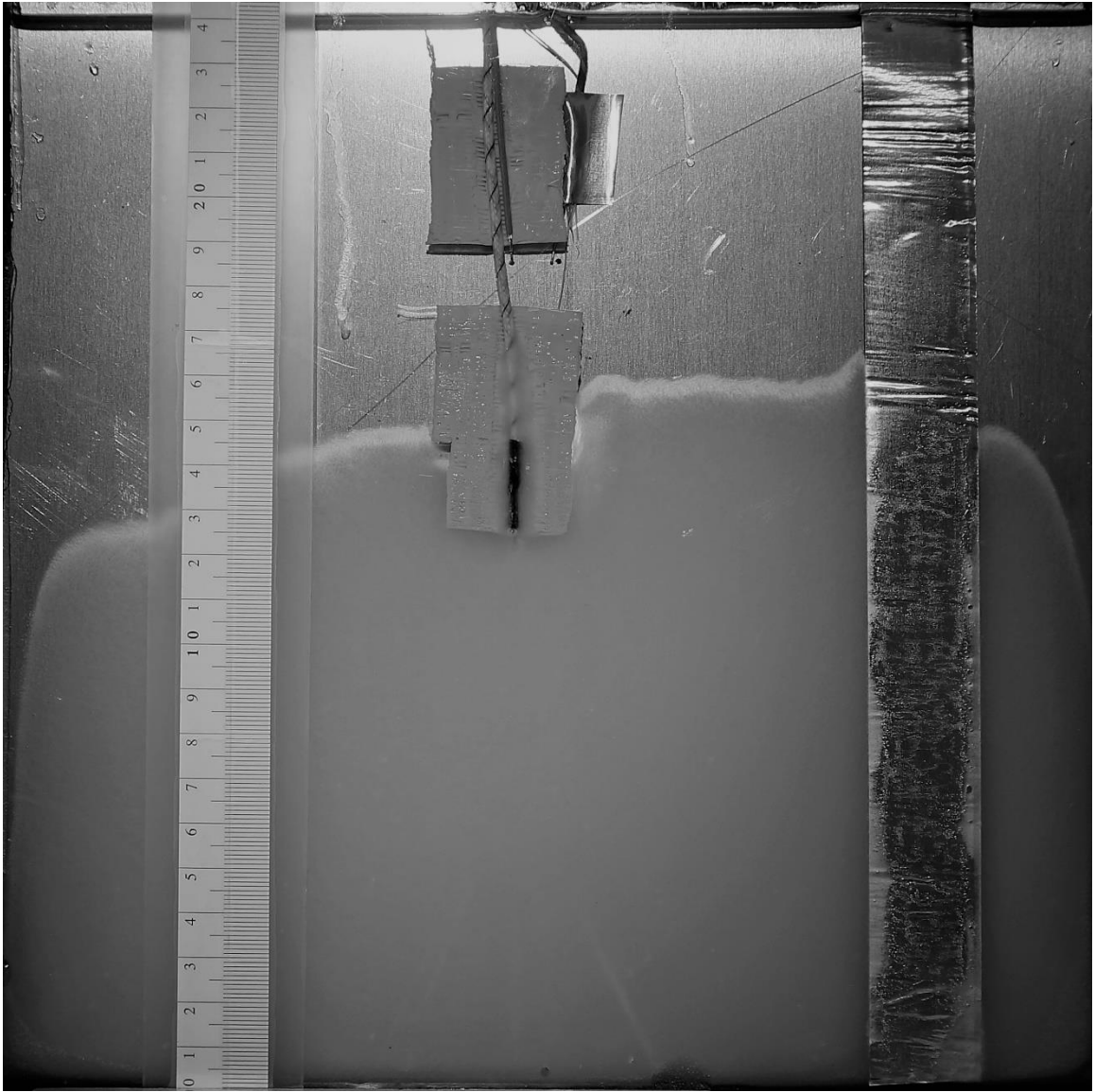
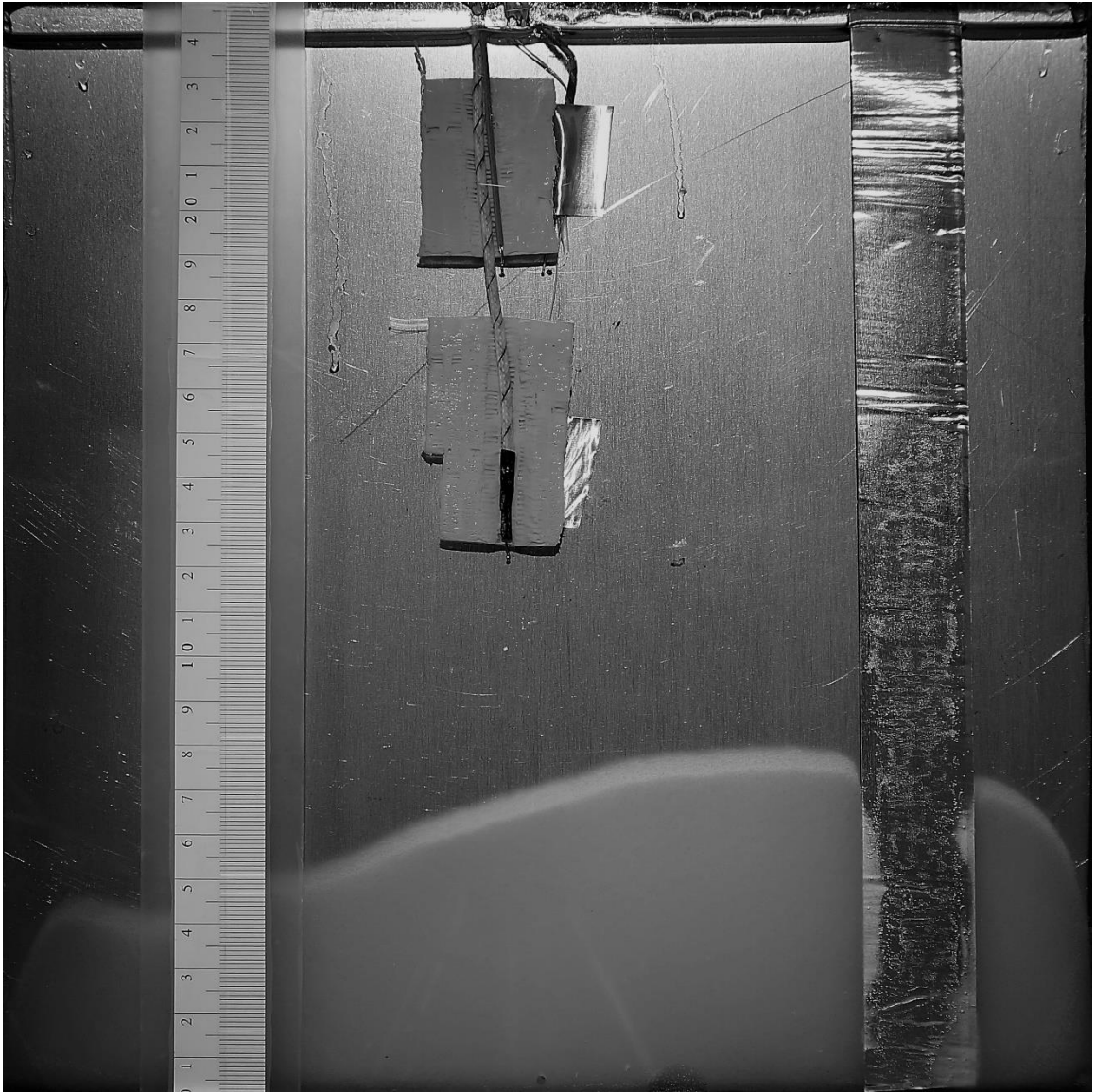
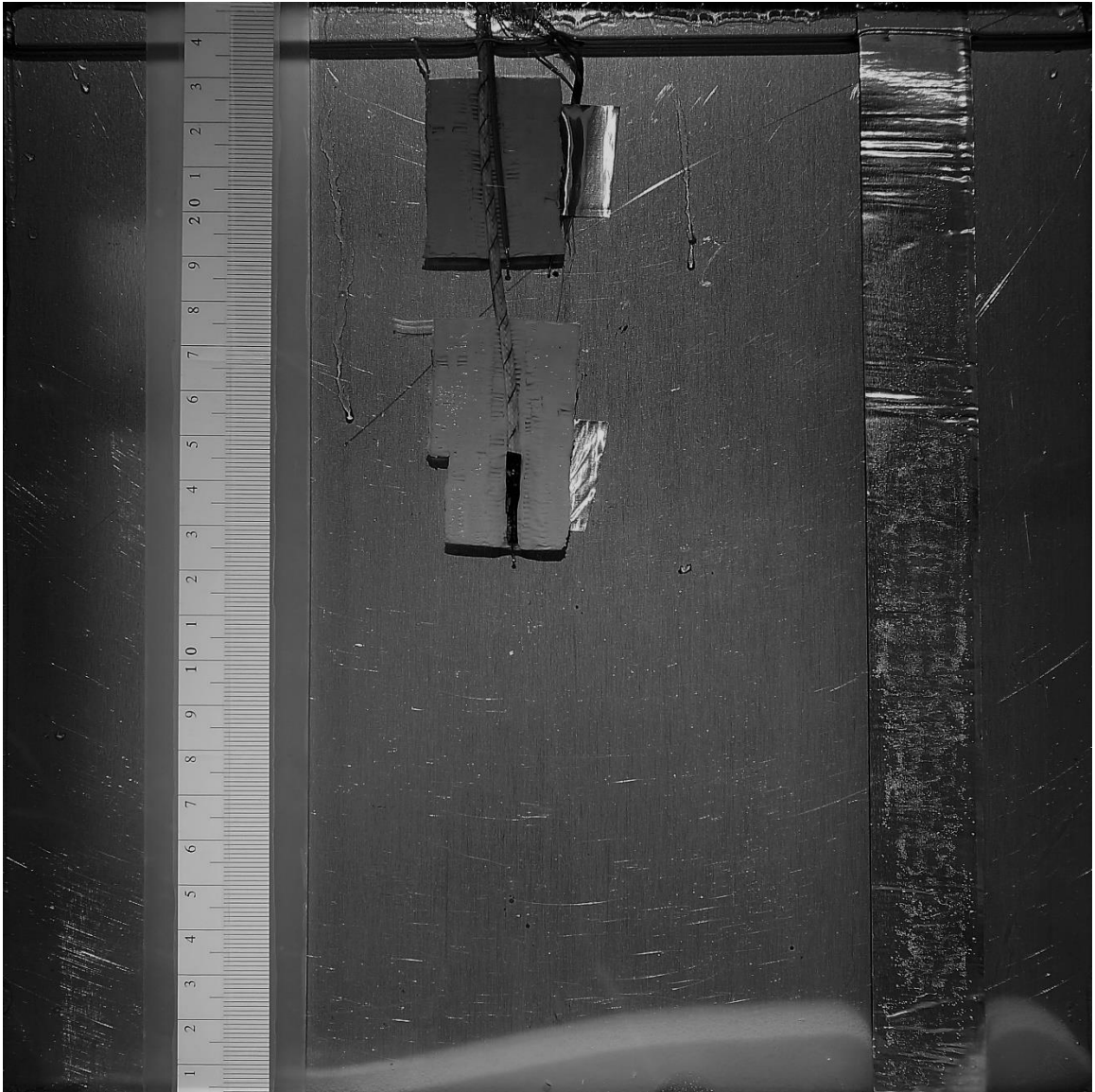


Figure 16: Solid-liquid boundary at  $t = 60$  min (Collector #2, vertical).



**Figure 17: Solid-liquid boundary at  $t = 70$  min (Collector #2, vertical).**



**Figure 18: Solid-liquid boundary at  $t = 80$  min (Collector #2, vertical).**

### **3.4.2 Collector 60° Inclined**

In contradiction with numerical results, the solid-liquid boundary progression in 60° inclined cycles was significantly retarded. No liquid region has been observed in the first 50 minutes of heating, and it took more than 120 minutes to become fully melted.

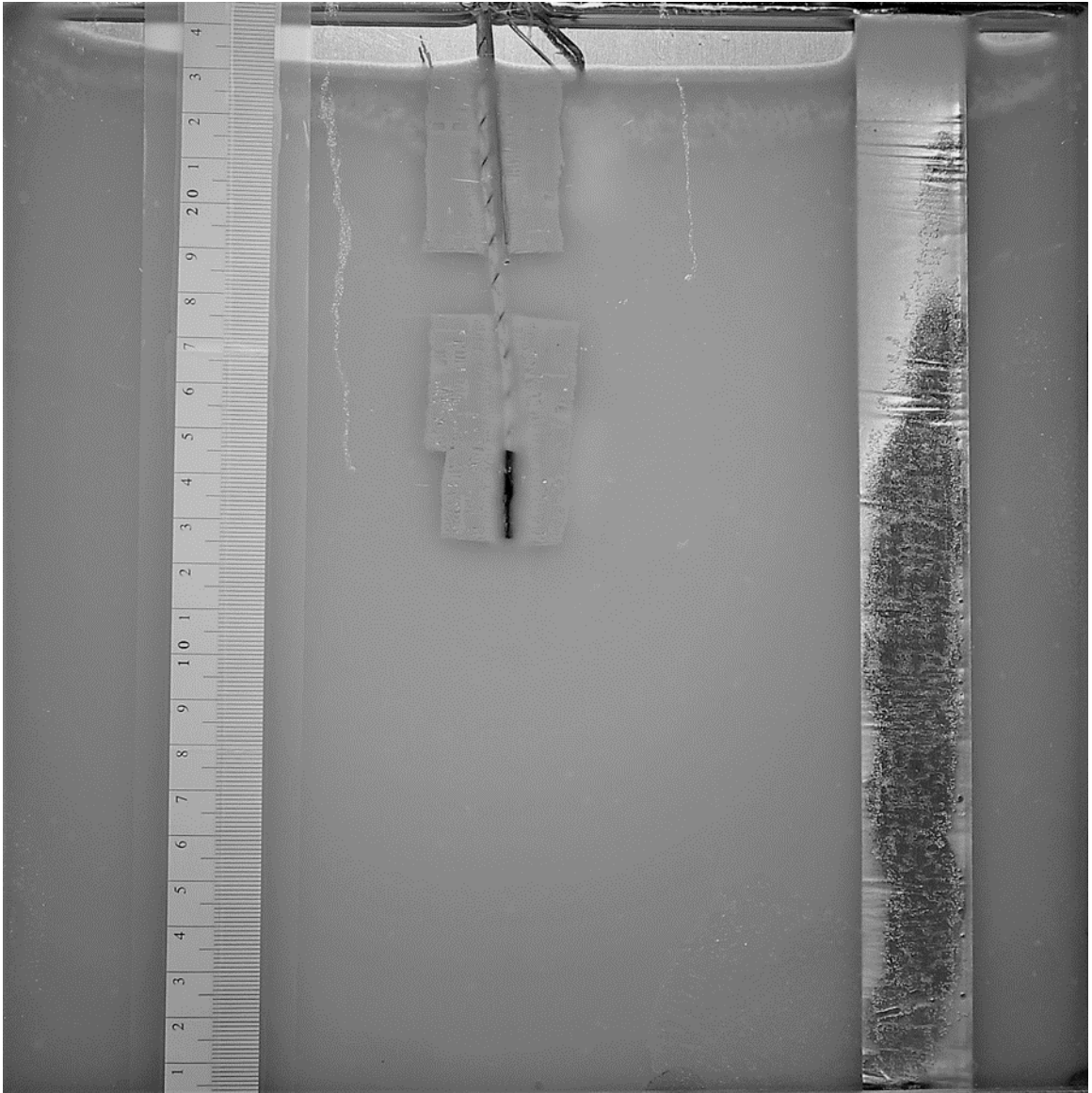


**Figure 19: Solid-liquid boundary at  $t = 60$  min (Collector #2,  $60^\circ$  Inclined).**

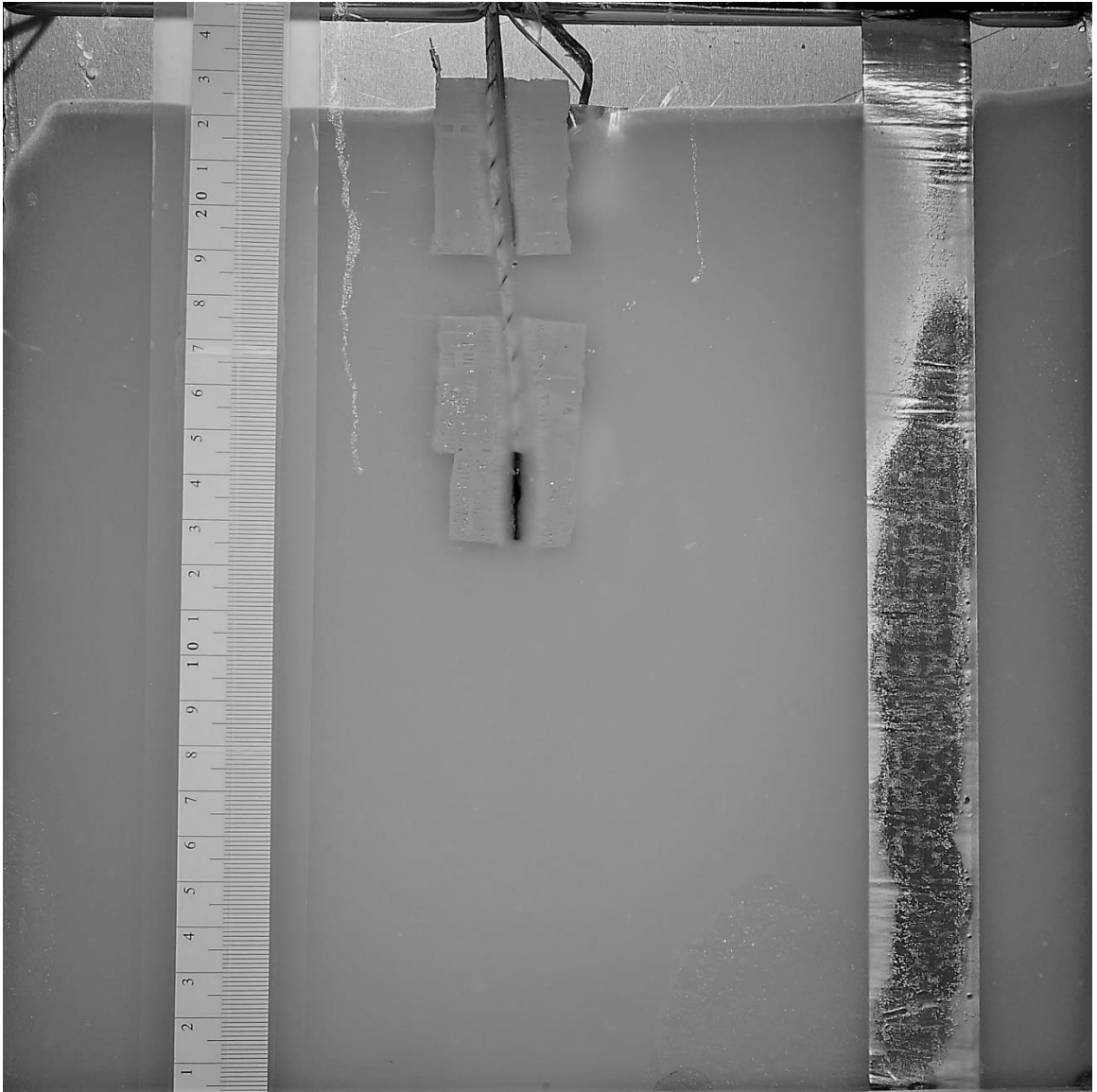


**Figure 20: Solid-liquid boundary at  $t = 70$  min (Collector #2,  $60^\circ$  Inclined).**

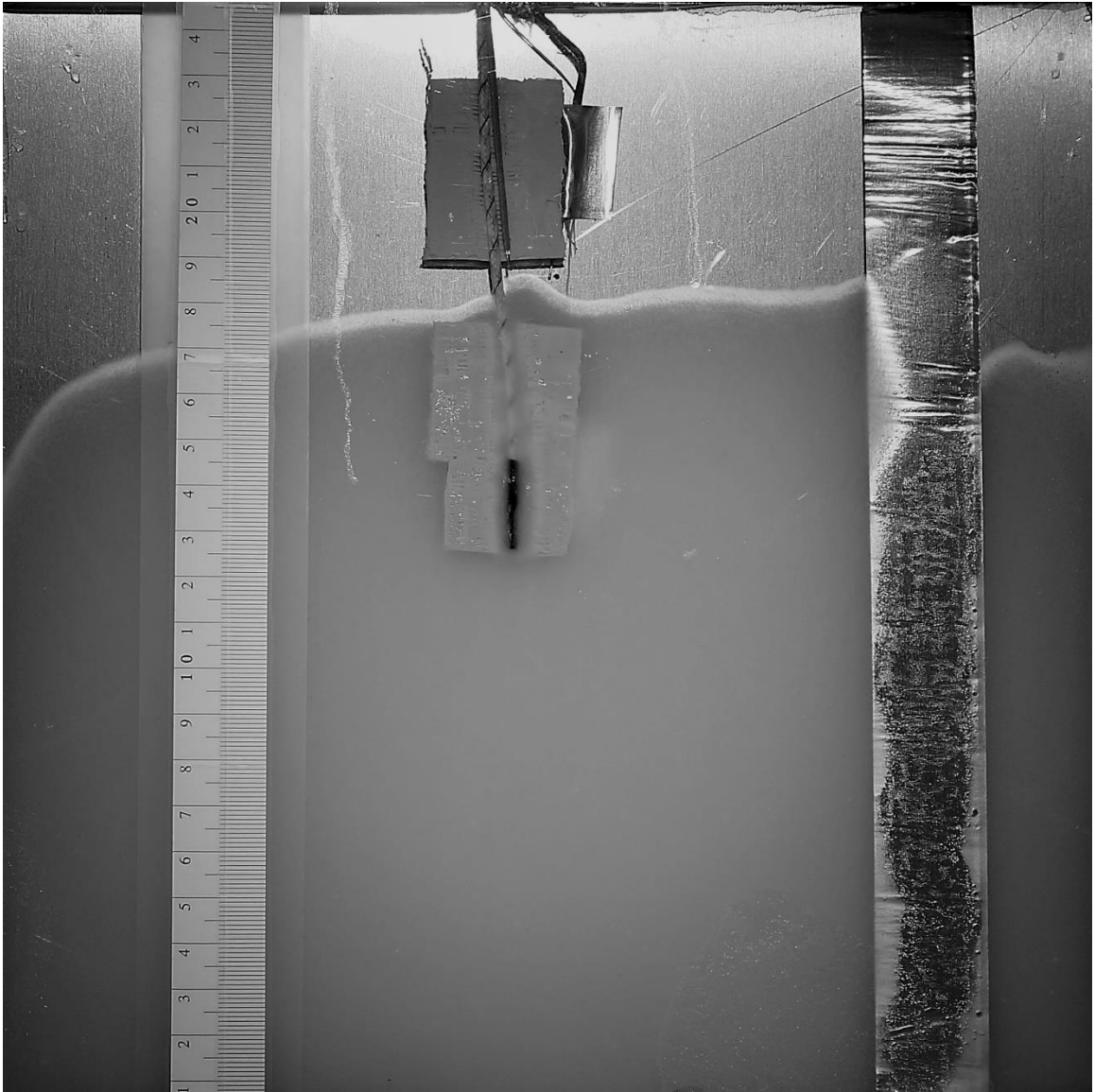


**Figure 21: Solid-liquid boundary at  $t = 80$  min (Collector #2,  $60^\circ$  Inclined).**

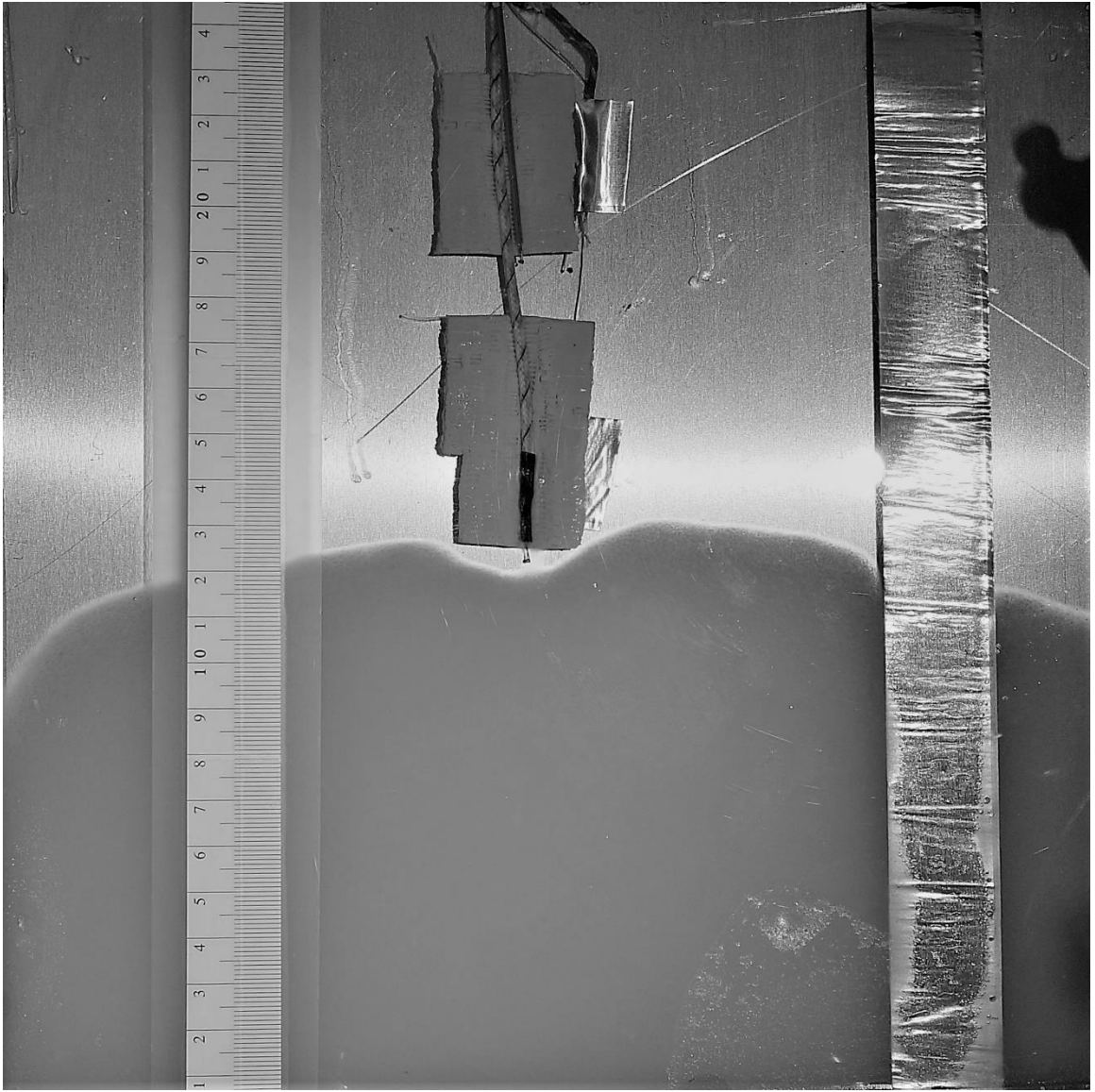


**Figure 22: Solid-liquid boundary at  $t = 90$  min (Collector #2,  $60^\circ$  Inclined).**

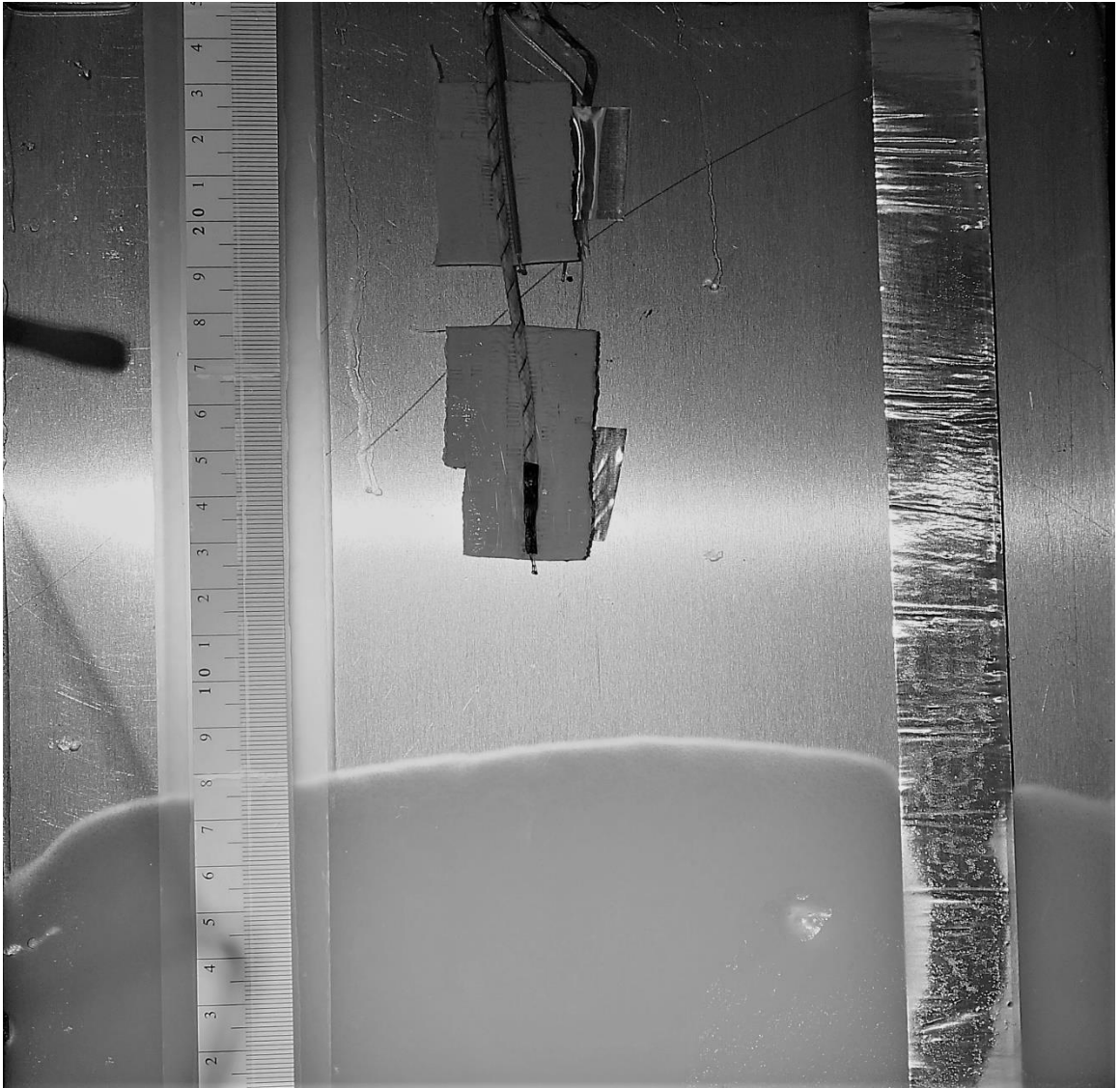


Figure 23: Solid-liquid boundary at  $t = 100$  min (Collector #2,  $60^\circ$  Inclined).

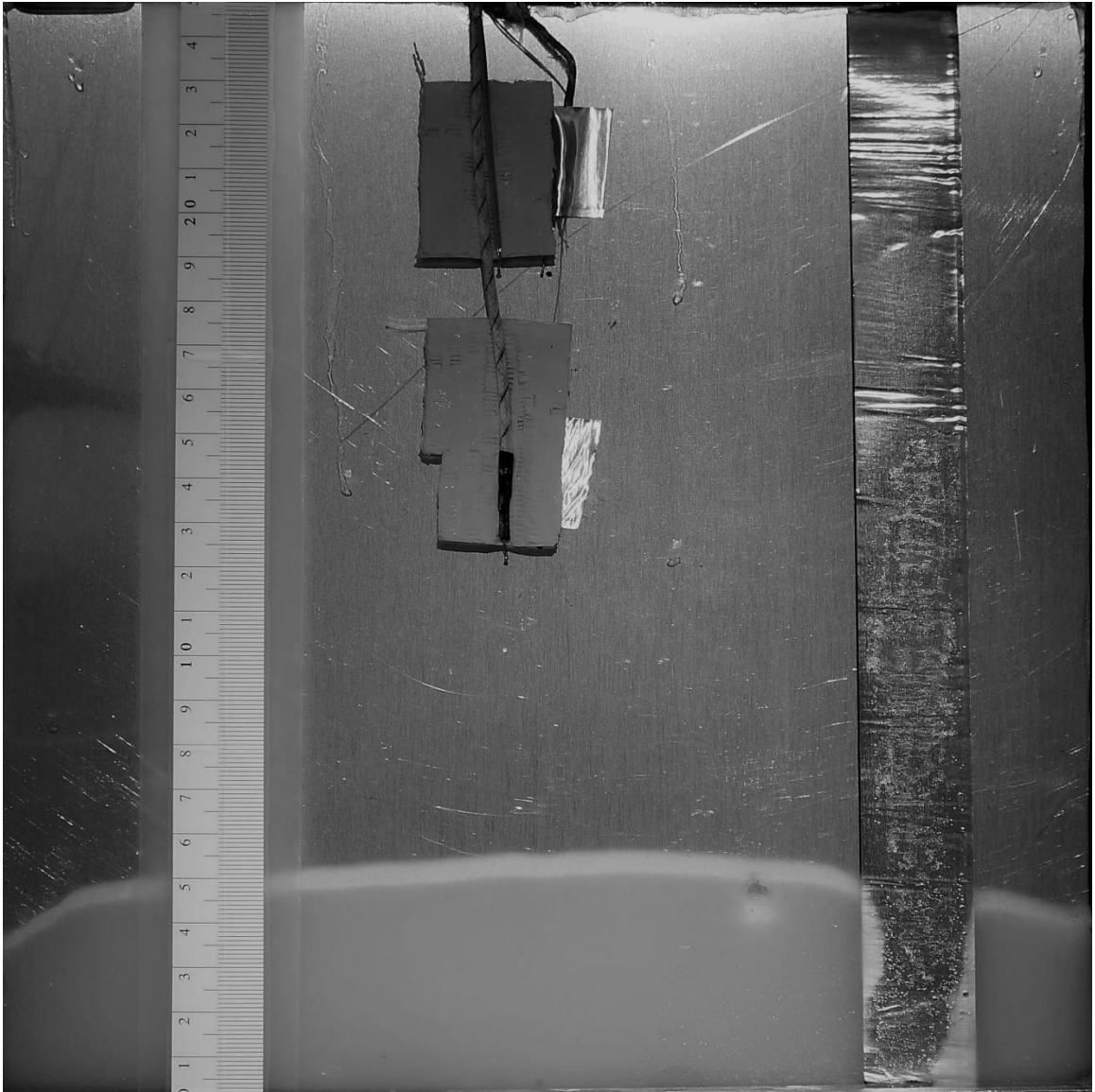


Figure 24: Solid-liquid boundary at  $t = 110$  min (Collector #2,  $60^\circ$  Inclined).

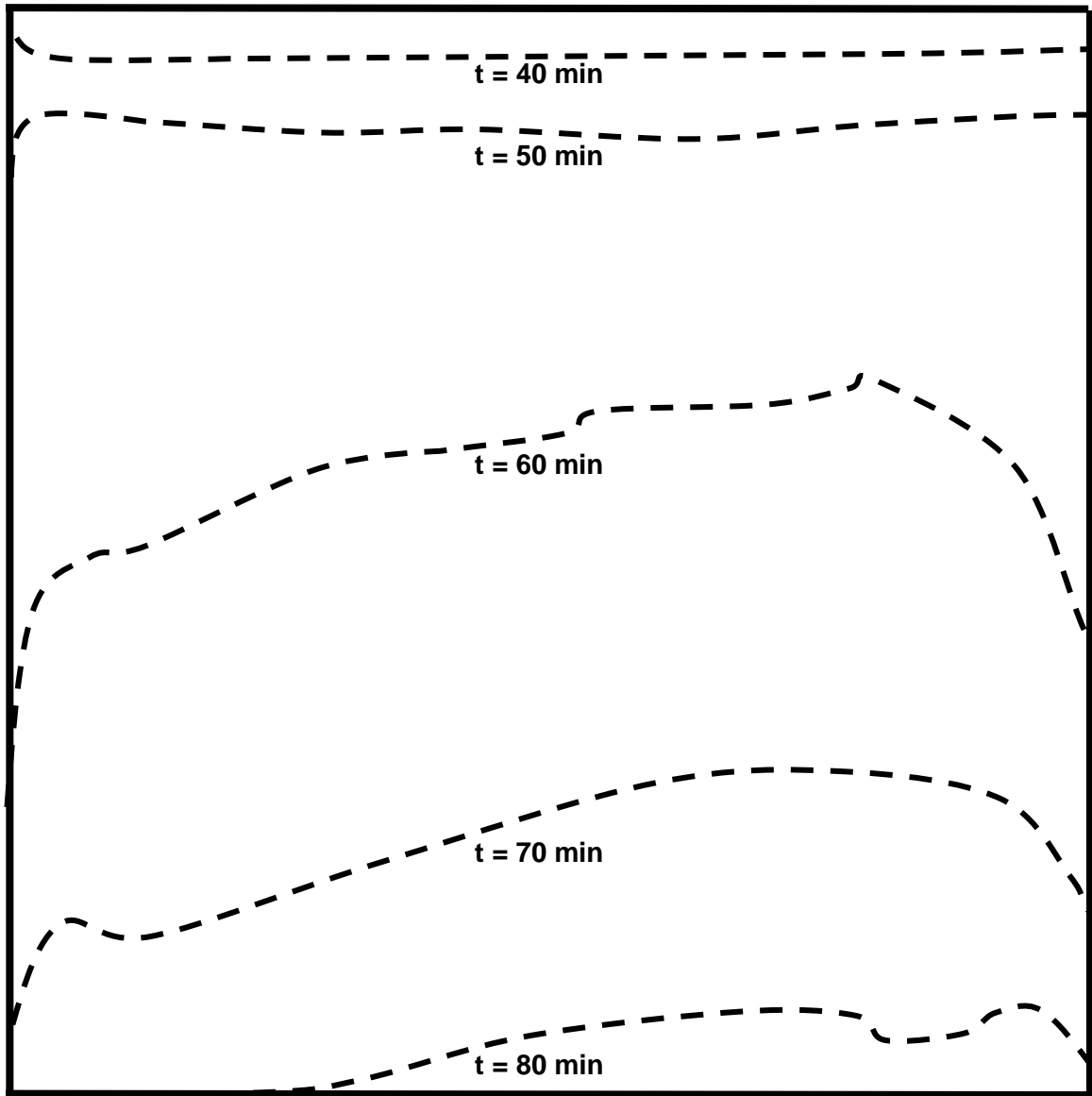


Figure 25: Evolution of solid-liquid boundary between  $t = 40$  min and  $t = 80$  min. (Collector#2, vertical).

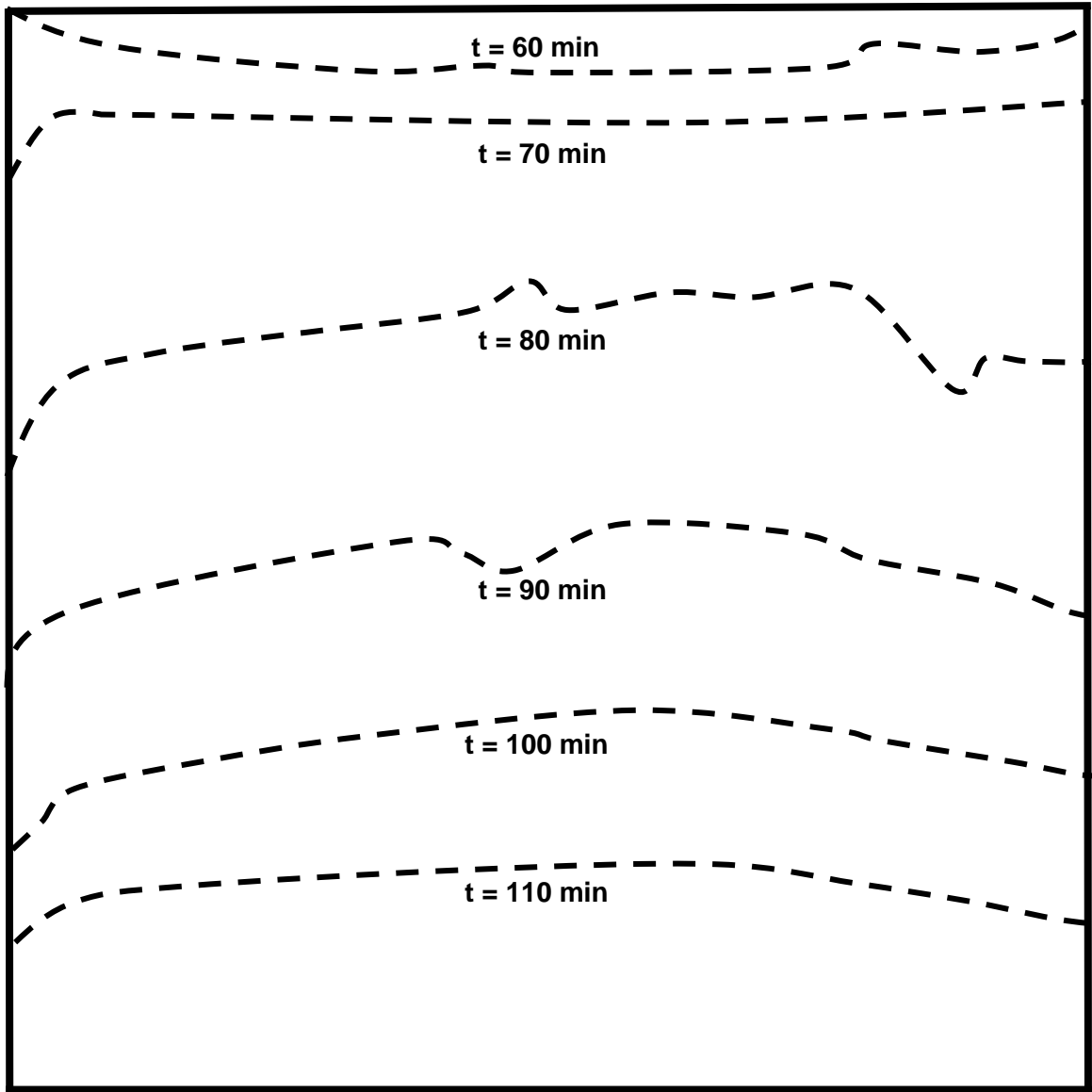


Figure 26: Evolution of solid-liquid boundary between  $t = 60$  min and  $t = 110$  min (Collector#2,  $60^\circ$  inclined).

### 3.4.3 Thermocouple Readings

The temperatures at points A and C were continuously increasing, but the rate is decelerating. This agrees with the increase of external heat loss, and eventually the temperature would reach its maximum where the inward heat flux (insolation) balances with heat loss (external natural convection).

On the other hand, the temperatures at points B and D tend toward constant near the melting range. The deceleration is related to the local phase transition process where the latent heat is absorbed for regrouping in molecular structure. Because the phase transition process is not isothermal, temperature rise is slowing down but not stopping. This phenomenon is less obvious at points A and C where the surrounding paraffin heated up quickly. A jump in temperature, although not always present, could be the effect of convection flow reaching the thermocouple.

There is also temperature gradient in  $x$ -direction, but the temperature gradient in  $y$ -direction is irregular.

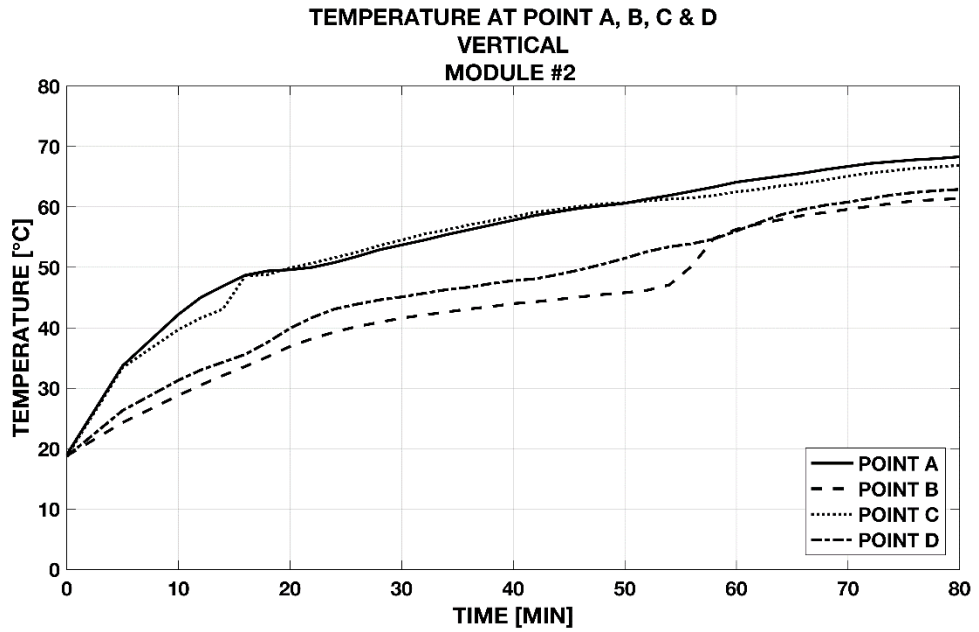
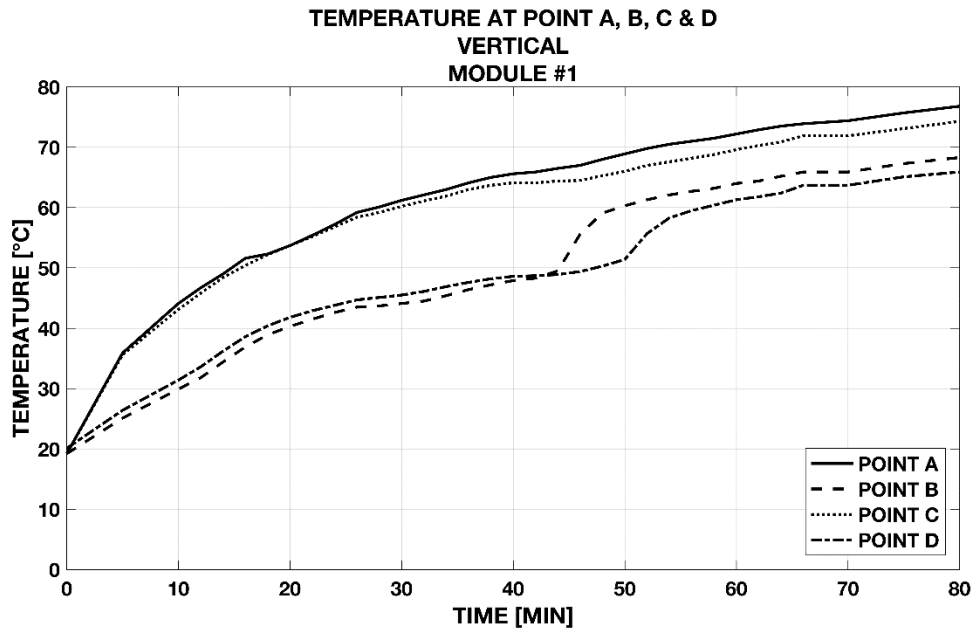


Figure 27: Temperature measurements of vertical oriented collector

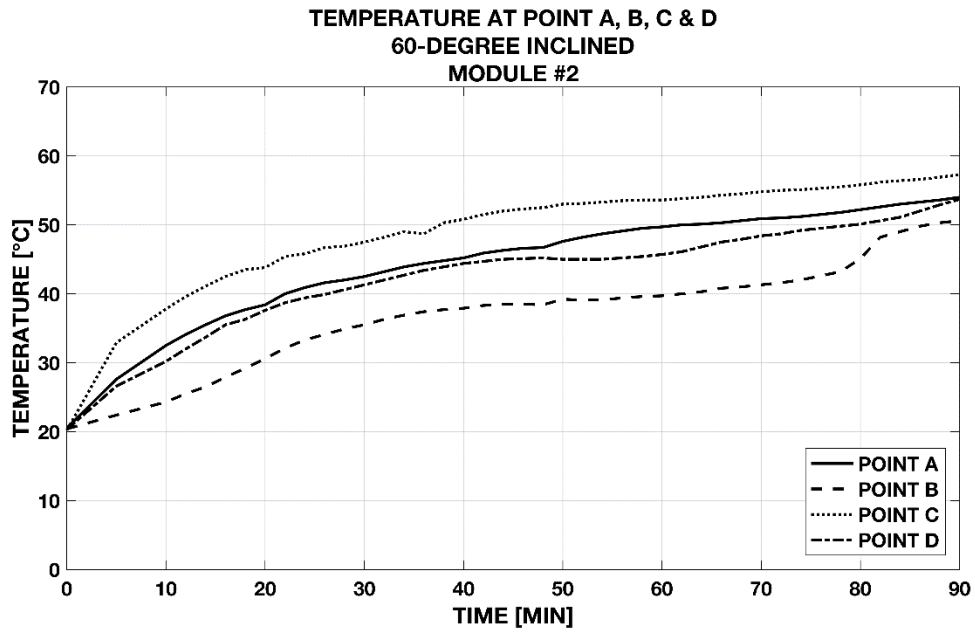
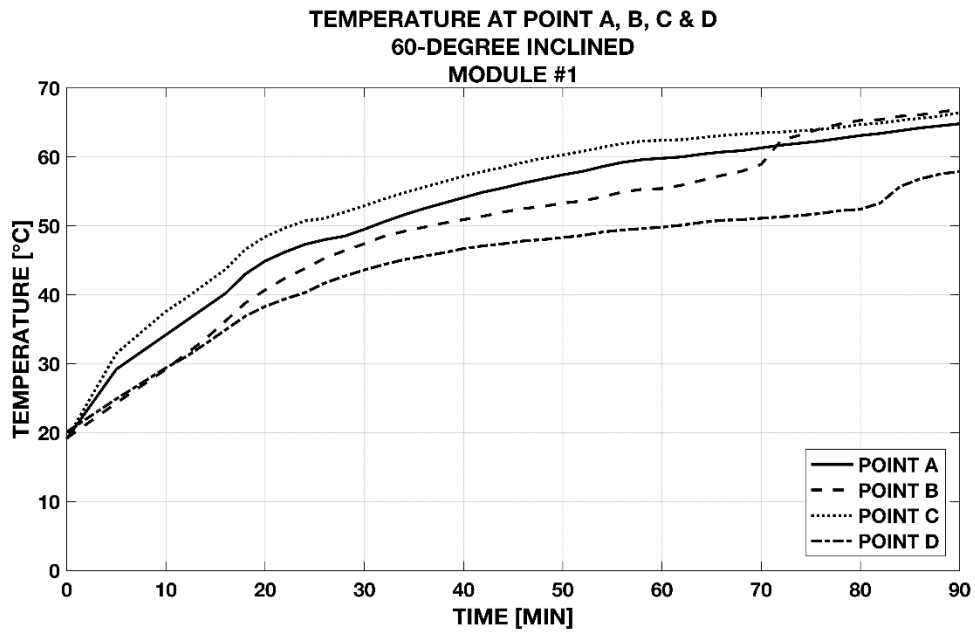


Figure 28: Temperature measurements of 60-degree inclination oriented collector

### 3.4.4 Comparison with Numerical Prediction

Figure 29 summarizes the predicted and measured progression of the solid-liquid boundary for two angular orientations of the collectors. The melting proceeds faster in the vertical orientation than in the 60-degree, shown in dots. By numerical approach, the two orientations generate no difference, shown in one solid line.

The correlations of Table 1 show only a small difference between convection coefficients in the vertical and inclined cases, though equations predict a 10% smaller value for the inclined plate. Considering the overall heat balance, a smaller convection coefficient on the upper surface would lead to a greater net amount of heat flowing into the collector. This would promote faster melting in the inclined case. However, convection effects in the melted paraffin within the collector would likely be more significant in the vertical case. The inaccurate parametric analysis of the external heat loss could be responsible. A definitive resolution of these competing effects is beyond the scope of the present work, and further exploration is recommended.

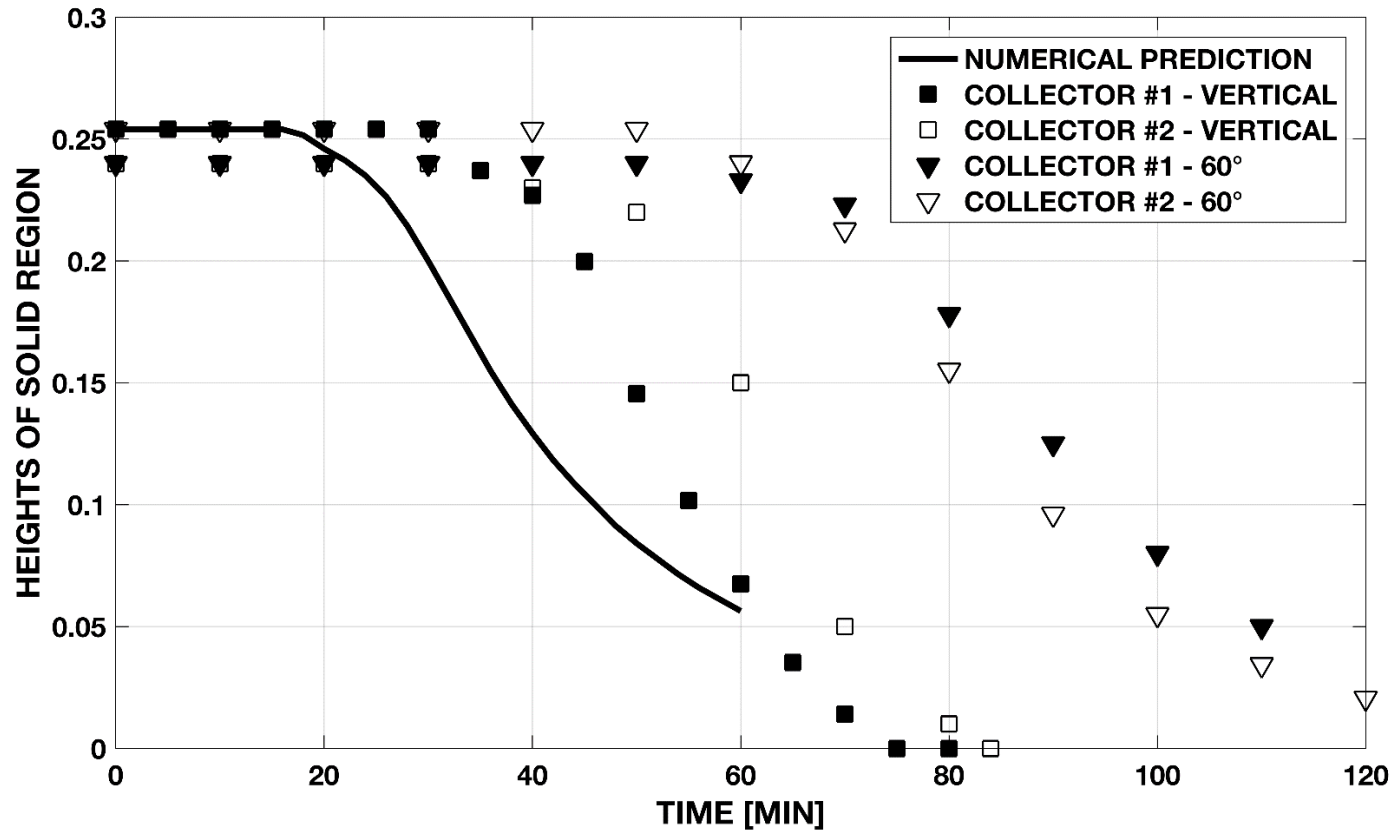


Figure 29: Prediction and measurements of the solid-liquid boundary progression.

## 4. Conclusion

Numerical and experimental studies were performed to illustrate the feasibility of a solar flat plate collector with integrated thermal storage using phase change material. For this study, a laboratory grade paraffin was chosen as PCM because its melting temperature near 50°C is well-suited to indoor space heating applications.

Experiments were conducted in the laboratory, using an array of lamps to approximate solar radiation. The constructed apparatus illustrates the feasibility of the solar flat plate collector with integrated heat storage in a reduced scale. Preliminary performance of the demonstration collector was measured with simulated insolation.

Measurements were taken in a vertical collector orientation as well as a 60 degree inclined position. Both computation and experiment were limited to the charging (melting) portion of the operation.

Numerically predicted trends of melting agreed with experiment, both showing an S-shaped curve of melt boundary position versus time, but some differences in the time scale between computation and experiment were noted. Calculation predicted more rapid melting in the middle of the time range, but at the end of a 60 minute period, both calculation and experiment indicated that slightly greater than 80% liquid fraction was achieved in the vertical case.

Experiments in the inclined case showed a slower progression of the melt front, with 80% liquid fraction occurring near 110 minutes, though calculation indicated no

difference. Considering the thermocouple readings which indicate a lower temperature rise in inclined tests, the discrepancy might result from unmodeled effects of inclination on external convection heat loss.

The results overall confirm that a solar flat plate collector with integrated phase change storage that can be charged on a time scale consistent with actual solar exposure is feasible.

#### ***4.1 Recommendations for Future Work***

To gain a deeper insight of the performances of a solar flat plate collector with integrated heat storage, some ways that may improve the validation experiments based on present work are listed below:

1. Measurements in natural sunlight.
2. Tests on larger scale collector.
3. Explore more angular orientation, especially small angles relative to the horizontal.
4. Investigate the effect of insolation incidence angle where the cosine effect reduces the incoming heat flux.
5. Extend the observations to discharging performance (solidification process)
6. Run test cycles with commercial grade paraffin, better to have the thermophysical properties fully characterized.
7. Visualize the buoyancy induced fluid flow in the cross-section plane.

## References

- [1] Fleischer, A. S. (2015). Thermal energy storage using phase change materials: fundamentals and applications. Springer.
- [2] Sharma, A., Tyagi, V. V., Chen, C. R., & Buddhi, D. (2009). Review on thermal energy storage with phase change materials and applications. *Renewable and Sustainable energy reviews*, 13(2), 318-345.
- [3] Schroder, J., & Gawron, K. (1981). Latent heat storage. *International Journal of Energy Research*, 5(2), 103-109.
- [4] Humphries, W. R., & Griggs, E. I. (1977). A design handbook for phase change thermal control and energy storage devices. NASA STI/recon technical report N, 78.
- [5] Maruoka (2002) Development of PCM for recovering high temperature waste heat and utilization for producing hydrogen by reforming reaction of methane
- [6] Dirand, M., Bouroukba, M., Chevallier, V., Petitjean, D., Behar, E., & Ruffier-Meray, V. (2002). Normal alkanes, multialkane synthetic model mixtures, and real petroleum waxes: crystallographic structures, thermodynamic properties, and crystallization. *Journal of Chemical & Engineering Data*, 47(2), 115-143.
- [7] Kenisarin, M. M. (2014). Thermophysical properties of some organic phase change materials for latent heat storage. A review. *Solar Energy*, 107, 553-575.
- [8] Sari, A., & Karaipekli, A. (2007). Thermal conductivity and latent heat thermal energy storage characteristics of paraffin/expanded graphite composite as phase change material. *Applied Thermal Engineering*, 27(8-9), 1271-1277.
- [9] Albert, M. R., & O'Neill, K. (1986). Moving boundary-moving mesh analysis of phase change using finite elements with transfinite mappings. *International Journal for Numerical Methods in Engineering*, 23(4), 591-607.
- [10] Voller, V. R., & Prakash, C. (1987). A fixed grid numerical modelling methodology for convection-diffusion mushy region phase-change problems. *International Journal of Heat and Mass Transfer*, 30(8), 1709-1719.
- [11] Tan, F. L., Hosseinizadeh, S. F., Khodadadi, J. M., & Fan, L. (2009). Experimental and computational study of constrained melting of phase change materials (PCM) inside a spherical capsule. *International Journal of Heat and Mass Transfer*, 52(15-16), 3464-3472.

- [12] Ma, L. (2017). Numerical Simulation on Performance Enhancement of Lead-Flow Partition Phase Change Heat Storage Unit. *Distributed Energy*, 2(3), 39-44 [In Chinese] 马林. (2017). 导流隔板式相变储热单元性能强化的模拟. *分布式能源*, 2(3), 39-44.
- [13] Tien, R. H., & Koump, V. (1970). Effect of density change on the solidification of alloys. *Journal of Heat Transfer*, 92(1), 11-16.
- [14] Maruoka, N., & Akiyama, T. (2003). Thermal stress analysis of PCM encapsulation for heat recovery of high temperature waste heat. *Journal of chemical engineering of Japan*, 36(7), 794-798.
- [15] Bareiss, M., & Beer, H. (1984). An analytical solution of the heat transfer process during melting of an unfixed solid phase change material inside a horizontal tube. *International Journal of Heat and Mass Transfer*, 27(5), 739-746.
- [16] Moore, F. E., & Bayazitoglu, Y. (1982). Melting within a spherical enclosure. *Journal of Heat Transfer*, 104(1), 19-23.
- [17] Christensen, C. (1983). *Advanced phase-change storage: analysis of materials and configurations* (No. SERI/TP-255-2018; CONF-830929-6). Solar Energy Research Inst., Golden, CO (USA).
- [18] National Renewable Energy Laboratory (NREL). [www.nrel.gov](http://www.nrel.gov)
- [19] L. Combelles, S. Lorente, R. Anderson, A. Bejan, Tree-shaped fluid flow and heat storage in a conducting solid, *J. Appl. Phys.* 11 (2012) 014902, <http://dx.doi.org/10.1063/1.3671672>.
- [20] H. Kobayashi, S. Lorente, R. Anderson, A. Bejan, Serpentine thermal coupling between a stream and a conducting body, *J. Appl. Phys.* 111 (2012) 044911, <http://dx.doi.org/10.1063/1.3689152>.
- [21] Bejan, A. (2013). *Convection heat transfer*. John wiley & sons.
- [22] Churchill, S. W., & Chu, H. H. (1975). Correlating equations for laminar and turbulent free convection from a vertical plate. *International journal of heat and mass transfer*, 18(11), 1323-1329.
- [23] Fujii, T., & Imura, H. (1972). Natural-convection heat transfer from a plate with arbitrary inclination. *International Journal of Heat and Mass Transfer*, 15(4), 755-767.

- [24] Zou, D. (2010). Numerical Simulation of the Heat Storage Process of A Waste Heat Utilization Oriented Phase Change Paraffin. *Journal of Engineering for Thermal Energy and Power*, 25(1). [In Chinese] 邹得球, 肖睿, 宋文吉, & 冯自平. (2010). 一种余热利用相变石蜡储热过程的数值模拟. *热能动力工程*, 25(1).
- [25] Yatabe, E. (1939). *The density and transition points of n-tetracosane* (Doctoral dissertation, University of British Columbia).
- [26] Rao, Z., Wang, S., & Peng, F. (2013). Self diffusion and heat capacity of n-alkanes based phase change materials: A molecular dynamics study. *International Journal of heat and mass transfer*, 64, 581-589.
- [27] Dirand, M., Bouroukba, M., Chevallier, V., Petitjean, D., Behar, E., & Ruffier-Meray, V. (2002). Normal alkanes, multialkane synthetic model mixtures, and real petroleum waxes: crystallographic structures, thermodynamic properties, and crystallization. *Journal of Chemical & Engineering Data*, 47(2), 115-143.
- [28] Rastorguev, Y. L., Bogatov, G. F., & Grigor'ev, B. A. (1974). Thermal conductivity of higher n-alkanes. *Chemistry and Technology of Fuels and Oils*, 10(9), 728-732.
- [29] Queimada, A. J., Quinones-Cisneros, S. E., Marrucho, I. M., Coutinho, J. A., & Stenby, E. H. (2003). Viscosity and liquid density of asymmetric hydrocarbon mixtures. *International Journal of Thermophysics*, 24(5), 1221-1239.
- [30] Lorente, S., Bejan, A., & Niu, J. L. (2014). Phase change heat storage in an enclosure with vertical pipe in the center. *International Journal of Heat and Mass Transfer*, 72, 329-335.
- [31] Anghel, E. M., Georgiev, A., Petrescu, S., Popov, R., & Constantinescu, M. (2014). Thermo-physical characterization of some paraffins used as phase change materials for thermal energy storage. *Journal of Thermal Analysis and Calorimetry*, 117(2), 557-566.
- [32] Mehling H, Cabeza LF. Heat and cold storage with PCM. Heat and Mass Transfer. Berlin Heidelberg: Springer Verlag; 2008.
- [33] Zhou, G., & Pang, M. (2015). Experimental investigations on thermal performance of phase change material Trombe wall system enhanced by delta winglet vortex generators. *Energy*, 93, 758-769.
- [34] Yuan, W., & Linhua, Z. (2006). Design of a new type of full-spectrum solar simulator. *Acta Energiæ Solaris Sinica*, 27(11), 1132. [In Chinese] 王元, & 张林华. (2006). 一种新型全光谱太阳模拟器设计 (Doctoral dissertation).

[35] Sharma, A., Sharma, S. D., & Buddhi, D. (2002). Accelerated thermal cycle test of acetamide, stearic acid and paraffin wax for solar thermal latent heat storage applications. *Energy Conversion and Management*, 43(14), 1923-1930.

[36] Kheirabadi, A. C., & Groulx, D. (2015). The effect of the mushy-zone constant on simulated phase change heat transfer. In *ICHMT Digital Library Online*. Begel House Inc..

[37] Liu, G., & Ma, W. (1986). Metal halogenide-dysprosium lamp solar simulator. *Acta Energiae Solaris Sinica*, 7(4), 437. [In Chinese] 刘国新, & 马薇. (1986). 金属卤化物镝灯太阳模拟器 (Doctoral dissertation).